

# Complex Envelope Based Modems: A Tutorial

Dayan Adionel Guimarães

**Abstract**—The complex envelope or baseband-equivalent representation of passband functions is a well-developed theory, known to provide elegant and, in most cases, eased mathematical tractability to the analyzes of signals and systems. Although this theory is covered extensively in many textbooks, there are hidden concepts and applications of it, for example related to the fast simulation of communication systems and to the fundamentals for developing software-defined radios. This tutorial exposes these concepts using a differentiated didactic approach, aiming at contributing to the understanding about how to model, simulate and implement modems based on the complex envelope theory.

**Index Terms**—Complex envelope, digital modulation, simulation of communication systems, software-defined radio.

## I. INTRODUCTION

THE complex envelope representation theory [1]–[4] is a powerful mathematical tool for analyzing signals and systems in several areas of science, especially in electrical engineering and telecommunications, where it is used mainly to confer an easier mathematical tractability to the analyzes. It is also a powerful tool for providing insight on how to develop the related systems, and to implement faster computer simulations. More recently, the theory is being applied in the development of wireless communication systems whose design and operation are strongly dependent of software, the so called software-defined radios (SDRs).

Basically, in wireless communication systems, the complex envelope representation theory allows for handling passband (or bandpass) modulated signals and system equations, which normally involve the presence of high frequency carrier signals, using a simpler baseband (or lowpass) equivalent representation where the absence of the carrier facilitates mathematical tractability. Moreover, owed to the fact that the baseband equivalent signal contains lower frequency components, the sampling rates in simulations and digital signal processing can be reduced, thus fastening the associated computations.

The design and operation of SDRs also make extensive use of such theory, in this case shifting to the software most of the tasks before used to be performed in hardware, eventually conferring to the system a large degree of flexibility, compactness and reliability.

Although covered in several books and articles, many of the concepts regarding digital modulation and demodulation using the complex envelope representation theory are hidden

or difficult to understand, giving opportunities for alternative approaches, like the one adopted in this tutorial. Instead of covering the use of the theory to facilitate mathematical analysis of telecommunication signals and systems, a subject that is also well covered in many references, the tutorial addresses other key usages, namely, the basis for simulating digital modulators and demodulators (modems), and the basis for understanding how these modems are embedded in SDRs.

The tutorial is targeted to everyone who wants to acquire working understanding about the underlying theory, especially the practicing Engineers and the undergraduate and graduate students in telecommunications and related areas.

However, although the tutorial is concerned with fundamentals, it demands from the reader some knowledge about signals and systems, and about the basic digital communication theory.

It is also worth highlighting which topics this tutorial does not aim to address. It does not cover details on the principles of digital communications, whose basic and advanced material can be found for example in [5] and [3], respectively. It is also not targeted at addressing in detail the principles of sampling and simulation of communication systems, topics extensively covered in the literature, for example [1], [5]–[7]. The SDR technology is not covered in detail here as well; it is well presented for instance in [8]–[12].

The remainder of the tutorial is organized as follows. The complex envelope representation theory is concisely explained in Section II. Section III establishes the connections of this theory with SDRs and computer simulations. Section IV recalls some basic concepts about the generalized modulator and the maximum likelihood demodulator for passband and complex envelope signals. Several modems constructed according to the complex envelope representation theory are discussed in Section V. A simulation to address the performance of one of these modems over a fading channel is discussed in Section VI. Different facets of baseband and passband signal filtering are considered in Section VII. Section VIII concludes the work.

## II. COMPLEX ENVELOPE REPRESENTATION OF PASSBAND SIGNALS

Following the reasoning adopted in [5], grounded on the fundamentals deeply explored for instance in [1]–[4], the theory about the complex envelope representation of passband signals is shortly reviewed in this section, aiming at giving to this tutorial a self-contained character, establishing notation, and building connections with the subsequent topics.

Let  $s(t)$  be a continuous-time signal whose Fourier transform is  $S(f)$ . The direct and inverse Hilbert transforms of  $s(t)$  are respectively given by

$$\hat{s}(t) = \frac{1}{\pi} \int_{-\infty}^{\infty} \frac{s(\tau)}{t - \tau} d\tau, \quad (1)$$

D. A. Guimarães is with the National Institute of Telecommunications (*Instituto Nacional de Telecomunicações*, Inatel), Santa Rita do Sapucaí, MG, Brazil. E-mail: dayan@inatel.br

This work was supported in part by CNPq, Grant 308365/2017-8, and RNP, with resources from MCTIC, Grant 01250.075413/2018-04, under the Radiocommunication Reference Center (*Centro de Referência em Radiocomunicações*, CRR) project of the National Institute of Telecommunications (*Instituto Nacional de Telecomunicações*, Inatel), Brazil.

DOI: 10.14209/jcis.2020.4.

$$s(t) = -\frac{1}{\pi} \int_{-\infty}^{\infty} \frac{\hat{s}(\tau)}{t-\tau} d\tau. \quad (2)$$

Recalling that a convolution in the time domain corresponds to a multiplication in the frequency domain, and noticing in (1) that the Hilbert transform of  $s(t)$  is the convolution between  $s(t)$  and the function  $1/\pi t$ , then the Fourier transform pair  $1/(\pi t) \rightleftharpoons -j\text{sgn}(f)$  can be applied to yield

$$\hat{S}(f) = -j\text{sgn}(f)S(f), \quad (3)$$

where  $j = \sqrt{-1}$  and  $\text{sgn}(f)$  is the sign function defined as

$$\text{sgn}(f) = \begin{cases} 1, & f > 0 \\ 0, & f = 0 \\ -1, & f < 0 \end{cases}.$$

From (3) it can be seen that the Hilbert transform of  $s(t)$  corresponds to a phase shift of  $-90$  degrees for the positive frequencies of  $S(f)$  and a phase shift of  $+90$  degrees for the negative frequencies.

Another useful signal representation is the analytic part, or pre-envelope of  $s(t)$ , which is defined as

$$s_+(t) = s(t) + j\hat{s}(t), \quad (4)$$

from where, applying (3) and the definition of  $\text{sgn}(f)$ , it follows that

$$S_+(f) = S(f) + \text{sgn}(f)S(f) = \begin{cases} 2S(f), & f > 0 \\ S(0), & f = 0 \\ 0, & f < 0 \end{cases}. \quad (5)$$

Thus, the analytic function  $s_+(t)$  represents a complex-valued signal that has no negative frequency components.

Now, consider that  $s(t)$  is a passband signal, which means that its bandwidth is essentially confined in a given bandwidth that is small compared to its center frequency  $f_c$ . From (5), the analytic spectrum  $S_+(f)$  is centered about  $f_c$  and contains only positive frequencies. Then, using the frequency-shift property [5, p. 104] of the Fourier transform, the pre-envelope  $s_+(t)$  can be written as a shifted version of some baseband function (whose spectrum is centered about  $f = 0$ ) to the frequency  $f_c$ , that is,

$$s_+(t) = \tilde{s}(t)e^{j2\pi f_c t}, \quad (6)$$

where  $\tilde{s}(t)$  is the baseband signal defined as the complex envelope of  $s(t)$ , also known as the baseband-equivalent of  $s(t)$ , which in light of (4) can be written as

$$\begin{aligned} \tilde{s}(t) &= s_+(t)e^{-j2\pi f_c t} \\ &= [s(t) + j\hat{s}(t)] e^{-j2\pi f_c t}, \end{aligned}$$

or, equivalently,

$$s(t) + j\hat{s}(t) = \tilde{s}(t)e^{j2\pi f_c t}.$$

From this last equation it follows that since  $s(t)$  is real, it can be written as the real part of the right-hand side. The important concept of the complex envelope representation of the passband signal  $s(t)$  results from this fact, that is,

$$s(t) = \text{Re} \left[ \tilde{s}(t)e^{j2\pi f_c t} \right]. \quad (7)$$

Notice that if  $s(t)$  is written in terms of some co-sinusoidal carrier, which is usually the case, its complex envelope representation becomes consistent with the Euler's formula  $e^{jx} = \cos(x) + j\sin(x)$ , since  $\cos(x) = \text{Re}[e^{jx}]$ , where  $\text{Re}[\cdot]$  denotes the real part of the argument. Analogously, the relation  $\sin(x) = \text{Re}[-je^{jx}]$  can be used when the carrier is sinusoidal.

The complex envelope  $\tilde{s}(t)$  in Cartesian form is

$$\tilde{s}(t) = s_I(t) + js_Q(t), \quad (8)$$

where  $s_I(t)$  and  $s_Q(t)$  are usually referred to as the in-phase (or direct) component and the quadrature component of  $\tilde{s}(t)$ , respectively. Since  $\tilde{s}(t)$  is a baseband function, then  $s_I(t)$  and  $s_Q(t)$  are also baseband functions.

Substituting (8) in (7), one obtains, after some straightforward simplifications, the important relation

$$s(t) = s_I(t) \cos(2\pi f_c t) - s_Q(t) \sin(2\pi f_c t). \quad (9)$$

The complex envelope (8) in the polar form is

$$\tilde{s}(t) = A(t)e^{j\theta(t)}. \quad (10)$$

Applying the complex envelope representation of  $s(t)$  given in (7) to the previous equation yields

$$\begin{aligned} s(t) &= \text{Re} \left[ A(t)e^{j\theta(t)} e^{j2\pi f_c t} \right] \\ &= A(t) \cos [2\pi f_c t + \theta(t)]. \end{aligned} \quad (11)$$

In this equation,  $A(t) = |\tilde{s}(t)|$  is the envelope of the passband signal  $s(t)$ , or its amplitude-modulated component, which can be expressed as a function of the in-phase and the quadrature components according to

$$A(t) = \sqrt{s_I^2(t) + s_Q^2(t)}, \quad (12)$$

and  $\theta(t)$  is the phase of  $s(t)$ , or its phase-modulated component, expressed in terms of the in-phase and the quadrature components as

$$\theta(t) = \arctan \left( \frac{s_Q(t)}{s_I(t)} \right). \quad (13)$$

The general form  $s(t) = A(t) \cos [2\pi f_c t + \theta(t)]$  can be used to represent several modulated signals. For instance, if  $A(t)$  is constant and  $\theta(t)$  assumes  $M$  equally spaced phases,  $s(t)$  becomes an  $M$ -ary phase-shift keying (MPSK) signal. If  $A(t)$  is constant and  $\theta(t)$  varies piece-wise-linearly according to  $M$  symbol-dependent slopes,  $s(t)$  turns out to be an  $M$ -ary frequency-shift keying (MFSK) signal. On the other hand, if  $A(t)$  and  $\theta(t)$  assume  $M$  properly designed pairs of amplitudes and phases,  $s(t)$  can be cast as an  $M$ -ary quadrature amplitude modulation (MQAM) signal.

Applying the Euler's formula to (10), another useful relation arises, which is

$$\tilde{s}(t) = A(t) \cos[\theta(t)] + jA(t) \sin[\theta(t)], \quad (14)$$

meaning that

$$s_I(t) = A(t) \cos[\theta(t)] \quad (15)$$

and

$$s_Q(t) = A(t) \sin[\theta(t)]. \quad (16)$$

Finally, from (11) it can be found a useful rule for easily determining the complex envelope of a passband signal or system function, hereafter referred to as the golden rule:

Golden rule to find the complex envelope:

- 1) Let the passband function be written according to the general form  $s(t) = A(t) \cos [2\pi f_c t + \theta(t)]$ .
- 2) Write the complex envelope representation of  $s(t)$  as the real part of  $A(t)e^{j\xi(t)}$ , where  $\xi(t)$  is the whole argument of the cosine function, yielding  $s(t) = \text{Re}[A(t)e^{j2\pi f_c t + j\theta(t)}]$ .
- 3) Factor the exponential into the product of exponentials, keeping evident the term  $e^{j2\pi f_c t}$ , which results in  $s(t) = \text{Re}[A(t)e^{j\theta(t)}e^{j2\pi f_c t}]$ .
- 4) The complex envelope is everything multiplying  $e^{j2\pi f_c t}$ , that is,  $\tilde{s}(t) = A(t)e^{j\theta(t)}$ , which is indeed the polar form (10).
- 5) If the carrier signal is sinusoidal, meaning that  $s(t) = A(t) \sin [2\pi f_c t + \theta(t)]$ , then it follows that  $\tilde{s}(t) = -jA(t)e^{j\theta(t)}$ , since the complex envelope representation in this case is  $s(t) = \text{Re}[-jA(t)e^{j2\pi f_c t + j\theta(t)}]$ .

The complex envelope and the complex envelope representation of a passband signal or system can be also written in the frequency domain. This alternative is not explored in detail here, since the time-domain approach suffices for the purpose of this tutorial. For additional material, the interested reader can resort for instance to [1, Ch. 3] and [2, Ap. A].

### III. THE ROLE OF THE COMPLEX ENVELOPE IN SOFTWARE-DEFINED RADIOS AND SIMULATIONS

The complex envelope representation is key to understand the concepts behind the design of SDRs and the implementation of computer simulations of signals and systems. This is owed mainly to the fact that the complex envelope  $\tilde{s}(t)$  is an alternative baseband version of the passband signal  $s(t)$ , demanding lower sampling rates. This lower sampling rates in turn reduces the computational burden, speeding up simulations and making it feasible and fast the digital signal processing tasks that are necessary to build SDRs.

#### A. The complex envelope in SDRs

In the SDR framework, the signals  $s_I(t)$  and  $s_Q(t)$ , being baseband signals, allow for efficient processing in the digital domain, via digital signal processors (DSPs), field programmable gate arrays (FPGAs) or computers. For example, a given modulated signal can be generated digitally, and then converted into the analog domain using its complex envelope in the form of  $s_I(t)$  and  $s_Q(t)$ . These signals then feed an IQ modulator, which is the device responsible for generating  $s(t)$  from  $s_I(t)$  and  $s_Q(t)$ , via (9). Figure 1 illustrates this SDR based modulator, where the input signal can be digital or analog, representing the information-bearing signal. If the input signal is analog, it obviously goes through an analog-to-digital (A/D) conversion before digital processing.

The spectrum translation from baseband to passband, which is realized by the sine and cosine carrier modulations in Fig. 1, can be made directly or in two steps: from baseband to an intermediate frequency (IF), and then from IF to passband. In the digital domain, this translation is typically made by a digital up-converter (DUC) device [13, Ch. 13] [14, Ch. 12].

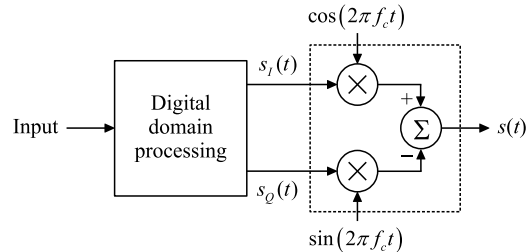


Fig. 1. Simplified block diagram of an SDR modulator. The block marked in dashed line is usually referred to as the IQ modulator.

The analogy applies to the passband received signal, which is typically an impaired version of  $s(t)$ : The received in-phase and quadrature baseband signals that are subsequently processed in the digital domain are obtained by passing  $s(t)$  through an IQ demodulator followed by appropriate low-pass filters (LPFs). Figure 2 illustrates this SDR based demodulator approach, where for didactic reasons it has been assumed that the received signal is not being corrupted by any impairment. However, even in this case, the recovered  $s_I(t)$  and  $s_Q(t)$  are not perfectly identical to the corresponding signals in the modulator given in Fig. 1, since the LPFs are not capable of eliminating the harmonic spurious resulting from the down-conversion from passband to baseband, and other distortions that may have been caused by hardware impairments and imperfections like phase noise, IQ phase and amplitude imbalances, DC-offset and nonlinear transfer characteristics of some device in the signal path [15].

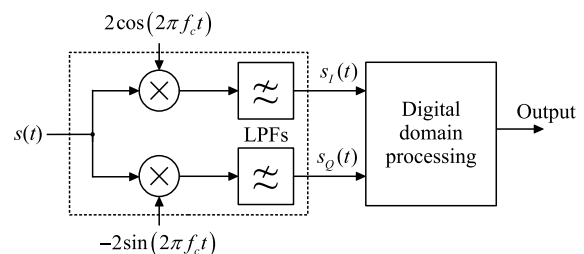


Fig. 2. Simplified block diagram of an SDR demodulator. The block marked in dashed line is usually referred to as the IQ demodulator.

In Fig. 2, the scaling of 2 and  $-2$  in the cosine and sine carriers compensate for the reduction to the half amplitude due to the IQ demodulation, and to the minus sign in the generation of the passband signal according to (9). The output of the diagram is the information-bearing digital or analog signal that is delivered to the destination.

Similarly to the case of an SDR transmitter, the spectrum translation from passband to baseband in the receiver, which is performed by the analog sine and cosine carrier demodulations in Fig. 2, can be made directly or in two steps, from passband to IF and then from IF to baseband. When the first option is

adopted, a direct-conversion receiver [16] takes place. In the SDR context, the direct or indirect translation to baseband is often implemented in the digital domain by a digital down-converter (DDC) [13, Ch. 13] [14, Ch. 12] [17]<sup>1</sup>.

Thus, it can be concluded that, in the worst case, only the radio-frequency (RF) part of the SDR must be implemented in conventional hardware with the present technology<sup>2</sup>.

### B. The complex envelope in simulations

One of the simplest ways to understand sampling, specifically the simplest case of uniform instantaneous sampling<sup>3</sup>, consists of realizing that sampling in time produces replicas of the spectrum of the original signal, located at integer multiples of the sampling frequency. Mathematically, let  $x(t)$  denote the signal to be sampled. The sampled signal  $x_s(t)$  is then

$$x_s(t) = x(t) \sum_{k=-\infty}^{\infty} \delta(t - kT_s), \quad (17)$$

where  $\delta(t)$  is the impulse function or delta de Dirac, and  $T_s = 1/f_s$  is the sampling period, with  $f_s$  being the sampling frequency. Given that the Fourier transform of an impulse train in time is an impulse train in the frequency domain, and that a multiplication in the time domain corresponds to a convolution in the frequency domain [5, p. 115], it follows that the spectrum of  $x_s(t)$  is

$$X_s(f) = \frac{1}{T_s} \sum_{k=-\infty}^{\infty} X(f - kf_s), \quad (18)$$

where  $X(f)$  is the Fourier transform of  $x(t)$ .

Figure 3 illustrates the sampling process in the frequency domain for a baseband signal, while Fig. 4 refers to a passband signal. The baseband signal is assumed to be confined<sup>4</sup> in  $(0, f_U)$  with  $f_U = 10$  Hz, and the passband signal is assumed to be within  $(f_L, f_U)$ , for  $f_L = 90$  Hz and  $f_U = 110$  Hz. Both signals are sampled at 80 samples per second.

In order to determine the location of the spectral replicas associated to the sampled signals, one firstly needs to remember that negative frequencies does not exist fiscally, but must be taken into account in signal analyzes. Hence, the center of the spectrum of both the baseband and the passband signals is 0 Hz (considering the negative halves that are not shown). The centers of the replicas in the sampled signal spectrum are located at  $kf_s = k80$  Hz, for  $k = 0, 1, 2, 3, 4, 5$  in the baseband signal, and for  $k = -1, 0, 1, 2, 3, 4, 5, 6$  in the passband signal.

<sup>1</sup>The author of [17] has other quite interesting articles closely related to signal processing for SDRs. These articles can be accessed in [18].

<sup>2</sup>The processing of RF or IF signals in the digital domain demands high speed digital-to-analog (D/A) and A/D converters, but it is already feasible at present in cases of not too high frequencies. As technology evolves, these devices will be pushed more and more towards the antennas of the wireless communication systems. Ideally, an SDR transmitter generates the signal to be applied to the power amplifier, which is connected to the transmitting antenna, and the SDR receiver samples and subsequently processes the signal coming from the low-noise amplifier (LNA) connected to the receiving antenna

<sup>3</sup>Uniform sampling means that the signal samples are equally spaced in time [9, p. 247]. Instantaneous sampling is the result of multiplying the signal to be sampled by an impulse train.

<sup>4</sup>The uncertainty principle of the Fourier transform [19] states that it is not possible to concentrate a function both in time and frequency. In other words, if it is needed to confine the signal spectrum in a given finite bandwidth, then the signal duration must go to infinite; analogously, if a signal is confined in a given finite time interval, then its bandwidth is infinite.

In Figs. 3(b) and 4(b), the numbers close to each spectral replica are the indexes  $k$ , and the letters denote the negative (n) and the positive (p) half of the original spectra given in (a). The frequency range of analysis in the present example is  $[0, 400]$  Hz, mimicking a simulation frequency of 800 Hz.

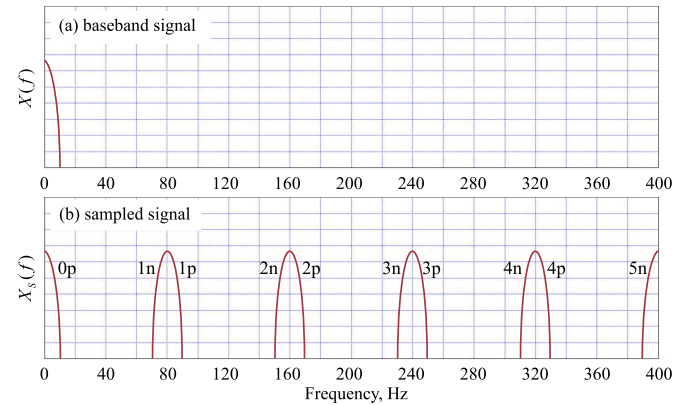


Fig. 3. Baseband sampling process in the frequency domain. Original baseband signal spectrum (a); sampled signal spectrum @  $f_s = 80$  Hz (b).

A first interesting aspect to be noticed in Figs. 3 and 4 is that the original spectra are present in the sampled signals, meaning that the original baseband or passband signals can be recovered by proper lowpass and bandpass filtering, respectively. However, taking into account that the signal spectrum is not strictly confined in practice, some sort of aliasing<sup>5</sup> will always remain. The smaller the sampling rate, the more severe will be the aliasing distortion.

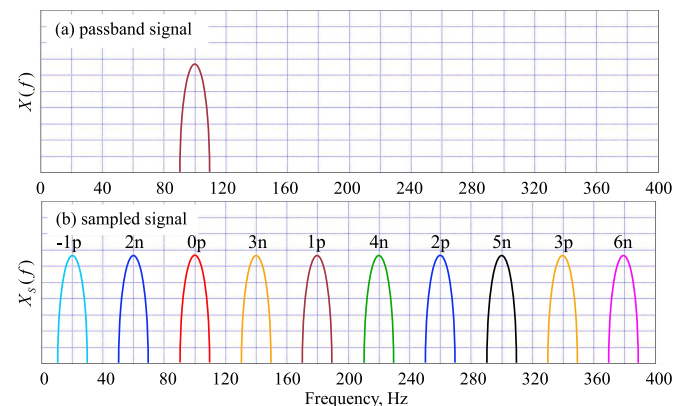


Fig. 4. Passband sampling process in the frequency domain. Original passband signal spectrum (a); sampled signal spectrum @  $f_s = 80$  Hz (b). Better viewed in color. Each color refers to a replica.

The uniform sampling theorem applied to baseband signals can be easily derived from Fig. 3. Notice that no aliasing occurs if the sampling frequency is equal to or larger than twice the upper limit of the baseband spectrum, that is

$$f_s \geq 2f_U. \quad (19)$$

<sup>5</sup>Aliasing refers to the superposition of the spectral replicas, which causes distortion in the desired portion of the spectrum. This distortion is usually referred to as aliasing distortion.

For the example in analysis, it means that any  $f_s \geq 20$  Hz is theoretically allowed in the case of the baseband signal.

The sampling theorem applied to a passband signal is considerably more intricate to derive. From [6], the condition of uniform sampling rates in this case is given by

$$\frac{2f_U}{n} \leq f_s \leq \frac{2f_L}{n-1}, \quad (20)$$

where  $n$  is the integer given by

$$1 \leq n \leq \left\lfloor \frac{f_U}{B} \right\rfloor, \quad (21)$$

where  $B = f_U - f_L$  is the passband signal bandwidth, and  $\lfloor x \rfloor$  is the largest integer no greater than  $x$ .

One can notice that the sampling frequency condition  $f_s \geq 2f_U$ , which is attained when  $n = 1$  in (20), specializes to the baseband sampling theorem. In other words, the baseband sampling theorem can be applied to passband signals, meaning that, for the example being discussed in this subsection,  $f_s \geq 220$  Hz, whose minimum is eleven times greater than the minimum in the case of the baseband signal.

Now consider that the lower limit of a passband spectrum is an integer multiple of the bandwidth, that is,  $f_L = cB$ . If  $c = n - 1$ , it follows from (20) that  $f_s = 2B$ , meaning that a passband signal  $s(t)$  can be sampled at a rate as low as the minimum sampling rate required for the baseband signal  $\tilde{s}(t)$ . However, the lower the sampling rate applied to  $s(t)$ , the more stringent are the requirements to avoid aliasing when compared to sampling  $\tilde{s}(t)$ , since the spectral replicas of the sampled passband signal get closer to each other faster than the ones associated to the baseband signal as the sampling frequency decreases, a phenomenon that becomes more pronounced for larger  $f_L/B$ ; see [6, Fig. 4]. This is readily noticed if the gaps between the spectral replicas in Figs. 3(b) and 4(b) are compared (recall that both the baseband and the passband signals were sampled with the same rate in this example).

Thus, in practice, the simulation sampling rate applied to  $s(t)$  must be sufficiently larger than the minimum one used to sample  $\tilde{s}(t)$ . This can be accomplished, for example, by applying the condition (20) assuming a guard band on the sides of the passband spectrum, as if it had a larger bandwidth (i.e., the reference values  $f_L$  and  $f_U$  are shifted to the left and to the right, respectively, without modifying the original spectrum). A detailed analysis of this and other concepts associated to the passband sampling are given in [6] and [9, Ch. 8].

#### IV. GENERALIZED MODULATOR AND MAXIMUM LIKELIHOOD DEMODULATOR

The signal-space representation theory [5, Ch. 5] is one of the most useful tools for developing and analyzing digital communication systems. It is grounded on the representation of a real symbol  $s_i(t)$ ,  $i = 1, \dots, M$ , confined in the interval  $T$  (i.e.,  $s_i(t)$  is an energy signal) and belonging to a given passband or baseband signaling, by means of a linear combination of orthonormal (i.e., orthogonal and normalized to unit energy) base functions  $\phi_k(t)$ ,  $k = 1, \dots, N$ , according to

$$s_i(t) = \sum_{k=1}^N s_{ik} \phi_k(t), \quad (22)$$

where the coefficients  $s_{ik}$  are computed using

$$s_{ik} = \int_0^T s_i(t) \phi_k(t) dt. \quad (23)$$

These coefficients can be interpreted as coordinates that can be grouped into the vectors  $\mathbf{s}_i = [s_{i1} \ s_{i2} \ \dots \ s_{iN}]^T$ , where the upper-script T denotes transposition. These vectors are usually referred to as signal-vectors, which define points in the  $N$ -dimensional Euclidean space. These points form the so-called signal constellation, which is the widely known geometric representation of digital communication signals.

The generalized modulator for any  $M$  and  $N$ , applicable to several modulation schemes, can be constructed according to (22), yielding the diagram shown in Fig. 5. The serial data bits  $\{b\}$  are grouped in blocks with  $\log_2 M$  bits that are serial-to-parallel (S/P) converted. These paralleled bits are converted into  $N$  coefficients by means of the look-up table (LUT). The subsequent blocks simply realize the operation (22).

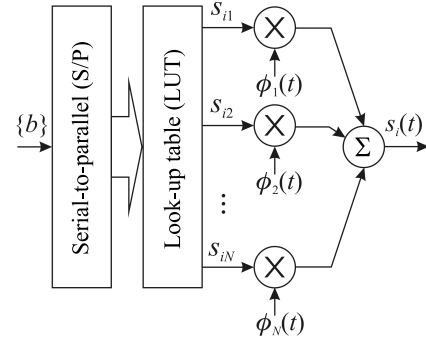


Fig. 5. Generalized modulator based on the signal-space theory [5, p. 371].

The maximum likelihood (ML) receiver [5, p. 384] is the one that minimizes the probability of a symbol error if the symbols are equally likely (which is the most common situation in practice). Hence, the ML receiver is optimum in this sense and is considered herein.

The derivation of an ML receiver is strongly dependent of the channel, mainly in what concerns the channel state information available to the receiver to feed the symbol decision process [20, Ch. 7]. For instance, a variety of receiver structures and performances can be achieved by adopting different combinations of channel state knowledge relating to the amplitude, phase, and delay parameter vectors associated with wireless fading channels [20, p. 189].

Unless otherwise mentioned, here it is considered the coherent ML receiver structure designed for the additive white Gaussian noise (AWGN) channel<sup>6</sup>, which suffices for the purpose of this introductory text. More advanced material can be found in [20], especially in its Chapter 7.

If a transmitted symbol  $s_i(t)$  is corrupted by additive white Gaussian noise  $w(t)$ , that is,  $x(t) = s_i(t) + w(t)$ , the generalized ML receiver is the one depicted in Fig. 6. The  $N$  correlators realize (23), with the difference that the samples

<sup>6</sup>The adoption of the pure AWGN channel model seems to be an oversimplification, but the digital communication theory tells that receivers designed for this channel can operate satisfactorily in fading environments if some sort of signal, transmitter or receiver diversity is applied, since diversity acts like a Gaussianization of the fading, i.e., a reduction of its variability [20, Ch. 7].

$x_k$  of their output signals are the corrupted versions of  $s_{ik}$  due to  $w(t)$ , that is,  $x_k = s_{ik} + w_k$ , where  $w_k$  is the result of passing  $w(t)$  through the  $k$ -th correlator.

It must be emphasized that in the present demodulator and in subsequent ones, the integrators that form the correlators are of the type integrate-and-dump, meaning that their output signals are reset to zero after each integration interval of  $T$  seconds. Moreover, the subsequent sampling processes, which are made at a rate of  $1/T$  samples per second, are of the type sample-and-hold (S&H), meaning that a given sample value is retained up to the next sampling instant.

The values of  $x_k$  in Fig. 6 are packed by the scalar-to-vector (S/V) block into the received vector  $\mathbf{x}$ , which is subsequently operated by inner products with the  $M$  signal-vectors. Half of the  $i$ -th symbol energy is then subtracted off the result of the  $i$ -th inner product, which acts as an energy compensation process [5, Sec. 5.8]. The estimated symbol  $\hat{m}$  is the one whose index corresponds to the largest energy-compensated quantity, which is equivalent to deciding in favor of the constellation signal-vector  $\mathbf{s}_i$  closest to the received vector  $\mathbf{x}$  in terms of Euclidean distance. The estimated symbol is finally mapped back into the estimated data bits  $\hat{b}$  that it represents.

The above passband generalized modulator and demodulator structures can be adapted to the design of many complex envelope based modems. To this end, firstly let (22) be written according to the complex envelope representation (7), yielding

$$\begin{aligned} \operatorname{Re} \left[ \tilde{s}_i(t) e^{j2\pi f_c t} \right] &= \sum_{k=1}^N s_{ik} \operatorname{Re} \left[ \tilde{\phi}_k(t) e^{j2\pi f_c t} \right] \\ &= \operatorname{Re} \left[ \sum_{k=1}^N s_{ik} \tilde{\phi}_k(t) e^{j2\pi f_c t} \right], \end{aligned} \quad (24)$$

where  $\tilde{s}_i(t)$  and  $\tilde{\phi}_k(t)$  are the complex envelopes of  $s_i(t)$  and  $\phi_k(t)$ , respectively<sup>7</sup>. Hence, it immediately follows that

$$\tilde{s}_i(t) = \sum_{k=1}^N s_{ik} \tilde{\phi}_k(t), \quad (25)$$

where

$$s_{ik} = \frac{1}{2} \operatorname{Re} \left[ \int_0^T \tilde{s}_i(t) \tilde{\phi}_k^*(t) dt \right]. \quad (26)$$

This last result comes from the fact that, given any two real signals  $z(t)$  and  $u(t)$ , and their complex envelopes  $\tilde{z}(t)$  and  $\tilde{u}(t)$ , respectively, then [21, p. 60]

$$\int_a^b z(t)u(t)dt = \frac{1}{2} \operatorname{Re} \left[ \int_a^b \tilde{z}(t)\tilde{u}^*(t)dt \right]. \quad (27)$$

Equation (25) unveils that the complex envelope based generalized modulator can be constructed according to the block diagram shown in Fig. 7, whose operation is analogous to the modulator shown in Fig. 5.

Regarding the complex envelope based demodulator, firstly recall from the signal-space theory that the inner products  $\mathbf{x}^T \mathbf{s}_i$  realized by the demodulator shown in Fig. 6 are equivalent to the correlations between  $x(t)$  and  $s_i(t)$ . Thus, in light of (27), these inner products can be expressed as

$$\mathbf{x}^T \mathbf{s}_i = \frac{1}{2} \operatorname{Re} \left[ \int_0^T \tilde{x}(t) \tilde{s}_i^*(t) dt \right], \quad (28)$$

<sup>7</sup>One must be aware that no normalization constant [21, p. 58] is being used in the present analysis, which means that the energy of a complex envelope is twice the energy of the corresponding passband function. As a consequence, the base functions  $\tilde{\phi}_k(t)$  form an orthogonal set with energy equal to 2 joules.

where  $\tilde{x}(t) = \tilde{s}_i(t) + \tilde{w}(t)$ , and where  $\tilde{x}(t)$ ,  $\tilde{s}_i(t)$  and  $\tilde{w}(t)$  are the complex envelopes of the real signals  $x(t)$ ,  $s_i(t)$ , and  $w(t)$ , respectively<sup>8</sup>. The remaining blocks of the complex envelope based demodulator are kept equal to the corresponding ones depicted in Fig. 6.

Alternatively, and more conveniently, the complex envelope based generalized demodulator can be constructed according to Fig. 8, where the structure shown in Fig. 6 has been maintained, with the correlators replaced by their complex envelope based versions. In this diagram and in subsequent ones, the single-line connections carry real signals, whereas the double-line connections carry complex-valued signals or vector-valued samples, depending on the context.

In practice, a connection carrying a complex-valued quantity is simply a two-way wiring, one carrying the real part and the other carrying the imaginary part (typically, no  $j$  is necessary). However, one must be aware when operating with such quantities, which must be done in the same way that a complex number is handled. For example, the multiplication between the real quantities  $(a, b)$  and  $(c, d)$ , which is equivalent to  $(a + jb)(c + jd)$ , yields two real values, namely  $(ac - bd)$  corresponding to the real part of the result, and  $(ad + bc)$  corresponding to its imaginary part. Similarly, the convolution  $(a + jb) * (c + jd)$  yields  $(a * c - b * d)$  for the real part of the result and  $(a * d + b * c)$  for the imaginary part.

## V. COMPLEX ENVELOPE BASED MODEMS

This section presents the complex envelopes of some basic digital modulated signals, followed by block diagrams of the corresponding modems with coherent detection (except otherwise noted). Besides providing hints on how to implement simulations of complex envelope based modems, the section also contains the fundamentals for applying the associated theory in the design of SDR modems. Moreover, the presentation approach via block diagrams facilitates understanding and potentially facilitates the use of powerful software tools like the VisSim/Comm [22], the Matlab Simulink [23], [24], and the GNU Radio [25], [26], since the graphical user interface of these tools resembles a block-like structure.

### A. $M$ -ary frequency-shift keying (MFSK)

The MFSK is one of the most didactic-appealing modulations from the perspective of the complex envelope theory, since it can be exploited to verify several relations established in Section II. This is the main reason for addressing the MFSK modulation in the first place.

An MFSK signal is characterized by  $M$  orthogonal symbols with equal energies  $E$ , formed by  $M$  tones with frequencies spaced by an integer multiple of half of the symbol rate  $R = 1/T$ , where  $T$  is the symbol duration, in seconds [5, pp. 450-507]. When the separation between adjacent tones is  $1/T$ ,

<sup>8</sup>Strictly speaking, the white noise  $w(t)$  is not a passband signal, since it violates the definition regarding the spectrum concentration in a given bandwidth much smaller than the center frequency. Nonetheless, if it is assumed that the white noise is flat over all frequencies of interest in the passband signal  $s_i(t)$  and zero elsewhere,  $w(t)$  can be adequately modeled as a passband noise.

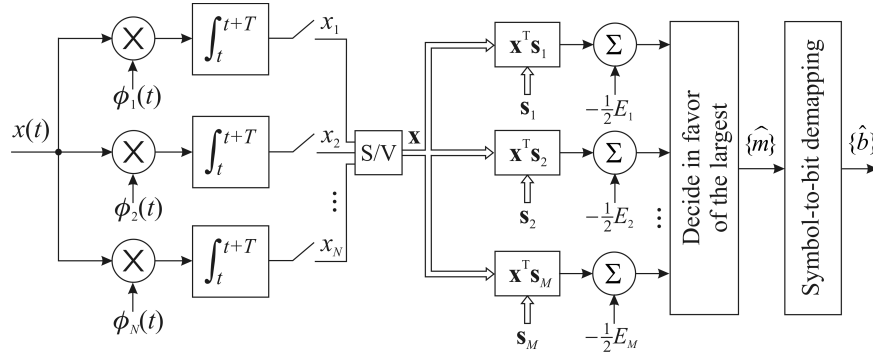


Fig. 6. Generalized ML demodulator over the AWGN channel, based on the signal-space theory [5, p. 384].

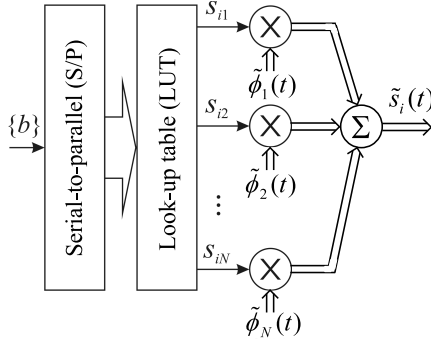


Fig. 7. Generalized complex envelope based modulator.

the implementation of the modulator and the demodulator becomes easier, since it is possible to guarantee a continuous-phase modulated signal by simply switching among the  $M$  tones, and it is possible to implement low-complexity symbol-by-symbol coherent or non-coherent detection schemes [5]. Hence, adopting this separation of  $1/T$ , the  $i$ -th  $M$ FSK symbol can be written as

$$s_i(t) = \sqrt{\frac{2E}{T}} \cos\left(2\pi f_c t + \frac{\pi a_i}{T} t\right), \quad (29)$$

for  $i = 1, \dots, M$ , where  $a_i \in \{\pm 1, \pm 3, \dots, \pm(M-1)\}$ , and  $f_c$  is the center frequency, which is the average of the tones whose frequencies are  $f_i = f_c + a_i/(2T)$  Hz.

Applying the golden rule for determining the complex envelope of a passband signal, as described at the end of Section II, it follows that

$$s_i(t) = \text{Re} \left[ \sqrt{\frac{2E}{T}} e^{j\frac{\pi a_i}{T} t} e^{j2\pi f_c t} \right],$$

meaning that the complex envelope of this  $M$ FSK signal is

$$\tilde{s}_i(t) = \sqrt{\frac{2E}{T}} e^{j\frac{\pi a_i}{T} t}, \quad (30)$$

or, equivalently,

$$\tilde{s}_i(t) = \sqrt{\frac{2E}{T}} \cos\left(\frac{\pi a_i}{T} t\right) + j \sqrt{\frac{2E}{T}} \sin\left(\frac{\pi a_i}{T} t\right), \quad (31)$$

from where the in-phase and the quadrature signals  $s_I(t)$  and  $s_Q(t)$  promptly arise according to (8).

The binary FSK (BFSK or 2FSK) is considered hereafter, since its simplicity facilitates presentation and understanding. Nevertheless, this simplified approach can be generalized to any  $M > 2$  with little effort.

The complex envelope of the 2FSK symbols with energy  $E = E_b$  and duration  $T = T_b$  is readily obtained from (31) using  $a_i \in \{\pm 1\}$ , which results in

$$\tilde{s}_i(t) = \sqrt{\frac{2E_b}{T_b}} \cos\left(\frac{\pi}{T_b} t\right) + j(-1)^i \sqrt{\frac{2E_b}{T_b}} \sin\left(\frac{\pi}{T_b} t\right), \quad (32)$$

where  $E_b$  is the average energy per bit and  $T_b$  is the bit duration, and where the relations  $\cos(\pm x) = \cos(x)$  and  $\sin(\pm x) = \pm \sin(x)$  have been applied.

If the tone with lower frequency is associated to a data bit 0, the corresponding symbol is  $\tilde{s}_1(t)$  and its frequency is  $f_1 = f_c - 1/(2T_b)$  hertz. Similarly,  $\tilde{s}_2(t)$  has the higher frequency  $f_2 = f_c + 1/(2T_b)$  hertz, representing a bit 1. Notice that the tone separation is  $1/T_b$  hertz.

Based on (32), Fig. 9 depicts the resultant 2FSK complex envelope based modulator.

The 2FSK complex modulator can be also constructed in light of (25) or according to Fig. 7, applying  $\tilde{s}_i(t) = s_{i1}\tilde{\phi}_1(t) + s_{i2}\tilde{\phi}_2(t)$ , for  $i = 1, 2$ , where  $s_{11} = \sqrt{E_b}$ ,  $s_{12} = 0$ ,  $s_{21} = 0$  and  $s_{22} = \sqrt{E_b}$ , using the base functions determined a little ahead in this subsection. In this case, the coefficients  $s_{11}$  and  $s_{12}$  are simultaneously generated when an input data bit 0 is applied to the modulator input, whereas  $s_{21}$  and  $s_{22}$  are generated for an input data bit 1.

Figure 10 shows waveforms of the 2FSK in-phase component  $s_I(t) = \sqrt{2E_b/T_b} \cos(\pi t/T_b)$  and the quadrature component  $s_Q(t) = \pm \sqrt{2E_b/T_b} \sin(\pi t/T_b)$  during 10 random bits, as well as the signal phase trajectory and the scatter-plot (xy plot) of  $s_I(t)$  versus  $s_Q(t)$ . From this figure it can be seen that the phase of the modulated signal changes continuously from symbol to symbol. It also illustrates the fingerprint of any FSK modulation, which is a circular scatter-plot.

The complex envelope based  $M$ FSK demodulator can be constructed according to Fig. 8. However, owed to the fact that the  $M$ FSK symbols form an orthogonal set, it means that  $N = M$  and, as a consequence, the demodulator will have  $M$  correlators followed by  $M$  inner products. The  $M$  base functions that feed the correlators are simply the normalized versions of the  $M$  symbols. This normalization is to unit

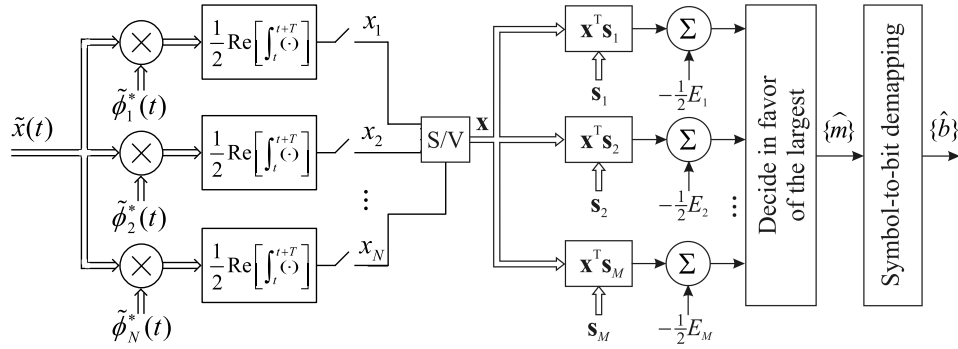
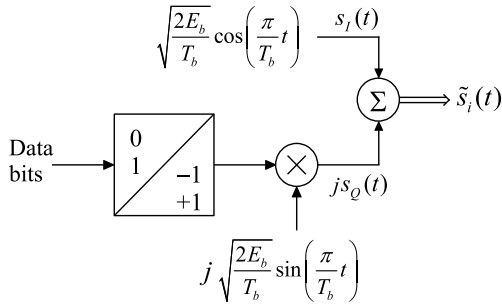
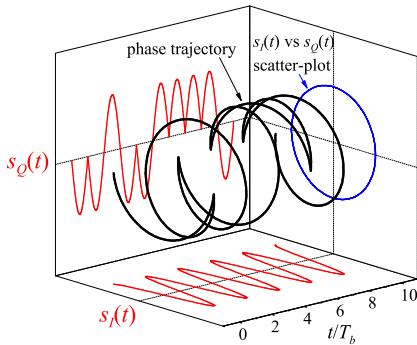


Fig. 8. Generalized complex envelope based ML demodulator over the AWGN channel.


 Fig. 9. 2FSK complex envelope based modulator considering a tone separation of  $1/T_b$  Hz.

 Fig. 10. Complex envelope, phase trajectory and scatter-plot of a 2FSK signal, considering the tone separation of  $1/T_b$  Hz. Better viewed in color.

energy in the case of  $\phi_k(t)$ , doubling in the case of  $\tilde{\phi}_k(t)$ , and is made by dividing  $s_i(t)$  or  $\tilde{s}_i(t)$  by  $\sqrt{E}$ .

It follows from (29), using the golden rule with  $M = 2$ , or directly from (32), that the complex envelopes of the base functions in the case of the 2FSK modulation are

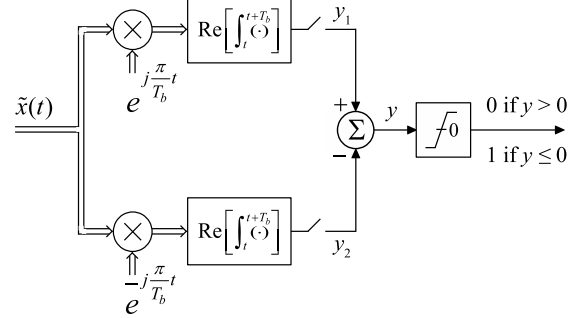
$$\begin{aligned}\tilde{\phi}_1(t) &= \sqrt{\frac{2}{T_b}} \cos\left(\frac{\pi}{T_b}t\right) - j\sqrt{\frac{2E_b}{T_b}} \sin\left(\frac{\pi}{T_b}t\right), \\ \tilde{\phi}_2(t) &= \sqrt{\frac{2}{T_b}} \cos\left(\frac{\pi}{T_b}t\right) + j\sqrt{\frac{2E_b}{T_b}} \sin\left(\frac{\pi}{T_b}t\right).\end{aligned}$$

Applying (28), the outputs of the inner products in the demodulator given in Fig. 8 become

$$\mathbf{x}^T \mathbf{s}_i = \frac{\sqrt{E}}{2} \operatorname{Re} \left[ \int_0^T \tilde{x}(t) \tilde{\phi}_i^*(t) dt \right].$$

Notice from this result that the inner products and the correlations with the base functions are redundant due to the fact that their results are a scale factor of one another. Moreover, since the *MFSK* symbols have equal energy, there is no need for making the subtractions of half their energies. Hence, the demodulator can be constructed by correlating the received signal with the complex conjugate of the base functions or with any scaled versions of them, and applying the results directly to the block that decides in favor of the symbol corresponding to the index of the largest result.

Thus, the complex envelope based 2FSK demodulator can be implemented according to Fig. 11, where the largest between  $y_1$  and  $y_2$ , which are scaled versions of  $x_1$  and  $x_2$ , respectively, is found by subtracting  $y_2$  from  $y_1$  and comparing the result with zero.


 Fig. 11. Complex envelope based 2FSK demodulator considering a tone separation of  $1/T_b$  Hz.

Another interesting simplification can be made in the complex envelope based 2FSK demodulator. Notice that the transmitted signals given in (32) differ only in their imaginary parts, which means that the demodulator can be built by correlating the imaginary part of  $\tilde{x}(t)$  with  $\sin(\pi t/T_b)$  and comparing the result with zero, as illustrated in Fig. 12.

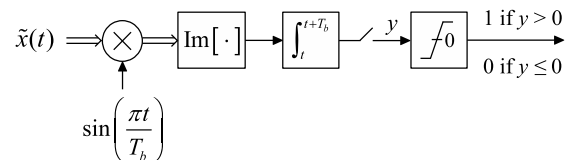


Fig. 12. Complex envelope based 2FSK demodulator alternative to Fig. 11.

This alternative yields the same performance of the demodulator given in Fig. 11. In order to verify this statement, assume  $T_b = 1$  and  $E_b = 1/2$  without loss of generality, which in (32) yields  $\tilde{s}_i(t) = \cos(\pi t) + j(-1)^i \sin(\pi t) = e^{j(-1)^i \pi t}$ . Additionally, consider that  $\tilde{w}(t) = w_I(t) + jw_Q(t)$ , where  $w_I(t)$  and  $w_Q(t)$  are sample functions of a lowpass AWGN process, each with power spectral density (PSD) of  $N_0/4$  watts/hertz. If the scaled base functions applied to the correlators in Fig. 9 are  $\tilde{\phi}_i(t) = e^{j(-1)^i \pi t}$ , it means that their energy are unitary. In this case, the variance of the noise present in  $y_1$  and  $y_2$  is  $N_0/4$ , implying that the noise variance in  $y$  is  $N_0/2$ . The means  $\bar{y}_1$  and  $\bar{y}_2$  are conditioned on the transmitted signal. If it is  $\tilde{s}_1(t)$ , then  $\bar{y}_1 = \text{Re}[\int_0^1 e^{-j\pi t} e^{j\pi t} dt] = 1$  and  $\bar{y}_2 = \text{Re}[\int_0^1 e^{-j\pi t} e^{-j\pi t} dt] = 0$ . Analogously, if the transmitted signal is  $\tilde{s}_2(t)$ , then  $\bar{y}_1 = 0$  and  $\bar{y}_2 = 1$ . Hence,  $\bar{y} \in \{\pm 1\}$ .

The bit error probability can be computed from the difference  $d$  between the two means of  $y$ , which is 2, and the variance  $\sigma^2$  of  $y$ , which is  $N_0/2$ , applying [5, p. 392],

$$P_b = \frac{1}{2} \text{erfc} \left( \frac{d}{\sqrt{8\sigma^2}} \right),$$

yielding  $P_b = (1/2)\text{erfc}(1/\sqrt{N_0})$  for the demodulator depicted in Fig. 11.

Regarding the demodulator shown in Fig. 12, given that the noise  $w_Q(t)$  has a PSD of  $N_0/4$  watts/hertz and the energy of  $\sin(\pi t)$  is 0.5 joule, the variance of the noise component in  $y$  turns out to be  $N_0/8$ . In terms of means, if the transmitted signal is  $\tilde{s}_1(t)$ , then  $\bar{y} = -\int_0^1 \sin(\pi t) \sin(\pi t) dt = -0.5$ . If the transmitted signal is  $\tilde{s}_2(t)$ , then  $\bar{y} = \int_0^1 \sin(\pi t) \sin(\pi t) dt = 0.5$ . Hence,  $\bar{y} \in \{\pm 0.5\}$ . Thus, the bit error probability of this demodulator is also  $P_b = (1/2)\text{erfc}(1/\sqrt{N_0})$ .

### B. Gaussian frequency-shift keying (GFSK)

Likewise the MFSK, the GFSK modulation exhibits interesting features that go from its mathematical model to the structures of the modulator and the demodulator, which are welcome to broaden the scope of this tutorial.

The GFSK applies a low-pass Gaussian pulse-shaping filter to the baseband symbol stream before continuous-phase FSK modulation, aiming at reducing the side-lobes of the PSD. It is adopted, for example, by the Bluetooth standard [27], [28], and is closely related to the Gaussian minimum-shift keying (GMSK) modulation [5, p. 521], which is the basic scheme adopted in the Global System for Mobile (GSM) standard. While the GMSK is binary and typically uses a modulation index  $h = \Delta_f T = 0.5$ , and a bandwidth by symbol duration product  $BT = 0.3$ , the GFSK is more flexible, for example adopting  $h = 0.5$  and  $BT = 0.5$  for the Bluetooth low energy (LE) standard, and  $h = 0.32$  and  $BT = 0.5$  or  $BT = 0.4$  for the Bluetooth basic rate and enhanced data rate (BR/EDR) standards, respectively. In the above parameters,  $\Delta_f$  is the frequency difference between the modulation tones, and  $B$  is the  $-3$  dB bandwidth of the Gaussian filter. Another characteristic of the GFSK modulation is that it can carry more than 2 symbols. For example, the Bluetooth standard adopts 2GFSK for 1 Mbit/s connections, and 4GFSK for 2 Mbit/s.

The GFSK signal can be expressed by means of the general form of an angle modulated<sup>9</sup> signal, that is,

$$s(t) = \sqrt{\frac{2E}{T}} \cos \left[ 2\pi f_c t + \frac{\pi h}{T} \int_{-\infty}^t b(u) du \right], \quad (33)$$

where  $h$  is the modulation index and  $b(t)$  is given by

$$b(t) = \sum_{n=-\infty}^{\infty} a_n g(t - nT),$$

and where  $a_n$  is a zero-mean multilevel sequence (bi-level in the 2GFSK and four-level in the 4GFSK). The function  $g(t)$  is a pulse with Gaussian-shaped rising and falling edges that results from the convolution between an unity-amplitude rectangular pulse of duration  $T$  and a Gaussian low-pass filter whose impulse response is

$$h(t) = \sqrt{\frac{2B^2\pi}{\ln 2}} \exp \left( -\frac{2\pi^2 B^2 t^2}{\ln 2} \right).$$

The effect of filtering is to smooth the phase shifts<sup>10</sup> associated to the frequency shifts. The product  $BT$  controls the trade-off between reducing the PSD side-lobes and penalizing the performance due to the intersymbol interference (ISI) caused by the time spread inherent to the Gaussian-filtered pulses [5, p. 523]. A large  $BT$  is associated to a small time spread, higher PSD side-lobes and better performances. A small  $BT$  is associated to a large time spread, lower PSD side-lobes and worse performances. Practical considerations regarding the Gaussian pulse shaping are reported for instance in [29]. Other aspects regarding the implementation of the GFSK modulation and demodulation are addressed in [30].

In the binary GFSK, which is considered hereafter, it is adopted  $E = E_b$ ,  $T = T_b$ , and  $a_n = \pm 1$  in (33) such that  $a_n = +1$  for the data bit 1 and  $a_n = -1$  for the data bit 0. Applying the golden rule to (33), the complex envelope of the binary GFSK signal is found to be

$$\tilde{s}(t) = \sqrt{\frac{2E_b}{T_b}} e^{j(\pi h/T_b) \int_{-\infty}^t b(u) du}, \quad (34)$$

from where  $s_I(t)$  and  $s_Q(t)$  are easily obtained based on (10), (15) and (16), giving rise to the binary GFSK complex envelope based modulator shown in Fig. 13, which can be seen as a direct synthesis of (34).

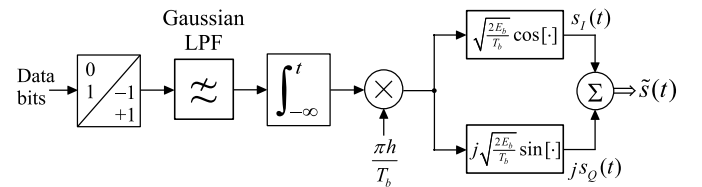


Fig. 13. Complex envelope based binary GFSK modulator.

<sup>9</sup>Notice that if  $h = 1$  in (33) and  $BT = \infty$  (i.e.,  $b(t)$  is a sequence of multilevel rectangular pulses of duration  $T$ ),  $s(t)$  specializes to the MFSK signal given in (29). Moreover, notice that an angle modulation is nonlinear, since it violates the principle of superposition of linear systems [21, p. 72]. Yet, if  $b(t)$  in (33) is an analog signal, a frequency modulation (FM) results.

<sup>10</sup>Recall that the instantaneous frequency of a signal is the derivative of the signal phase evolution over time, that is,  $f = (1/2\pi)d\theta(t)/dt$  hertz, if  $\theta(t)$  is expressed in radians.

Figure 14 shows waveforms of the in-phase and the quadrature components of a binary GFSK signal during 10 random bits, as well as the signal phase trajectory and the scatter-plot of  $s_I(t)$  versus  $s_Q(t)$ . It can be seen that the phase trajectory is continuous, likewise in the 2FSK modulation illustrated in Fig. 10, but is smoother than the one associated to the 2FSK, a consequence of the Gaussian-filtering before frequency-shift keying. It is also interesting to notice that the fingerprint of the GFSK modulation remains a circular scatter-plot, as expected.

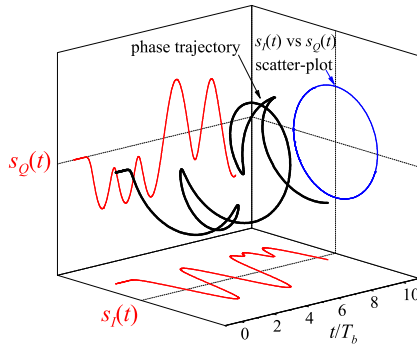


Fig. 14. Complex envelope, phase trajectory and scatter-plot of a binary GFSK signal, for  $BT_b = 0.5$  and  $h = 0.32$ . Better viewed in color.

The generation of a GFSK signal based directly on the generalized complex envelope modulator shown in Fig. 7 is not possible because the need of maintaining phase continuity in the modulated signal independent of  $h$ . Analogously, the construction of the GFSK demodulator does not follow the structure depicted in Fig. 8.

There are several GFSK demodulation structures and algorithms proposed in the literature; see for instance [31] and references therein. In the context of Bluetooth, most of them adopt non-coherent detection due to the need for low cost devices, for satisfactory performance with the frequency-hopping scheme, and to cope with different modulation indexes.

Here it is considered a phase-shift discriminator for demodulation, which basically reverts the operations established in (34). However, the performance of this solution may be poor due to the high levels of ISI produced by the pulse shaping, especially when  $BT$  is small. High performance penalties also may result if  $h$  is small, since this situation reduces the ability of discriminating the frequency shifts in the received signal. To improve performance, the phase-shift discriminator, or any other demodulation processes, often requires to be complemented with some sort of subsequent detection algorithm [31]. The optimum one, in the sense of minimizing the probability of deciding in favor of a wrong symbol sequence, is the maximum likelihood sequence detection (MLSD) [32].

Figure 15 presents the complex envelope based GFSK demodulator with a phase-shift discriminator. Considering a noiseless complex received signal for clarity, the leftmost block splits it in the real and imaginary parts, and the arctan operation gives a quantity proportional to the phase shift evolution over time, which corresponds to the right-hand side of the argument of the cosine in (33). The derivative yields a signal proportional to  $b(t)$ , which is the Gaussian-filtered symbol sequence. The use of a simple slicer with a zero

threshold would suffice to recover the data bits from this signal, but only for high  $BT$  values. Hence, the detection algorithm in Fig. 15 aims at remembering that this additional process might be needed to combat the high levels of ISI when  $BT$  is small, or to improve frequency discrimination when  $h$  is small, or both.

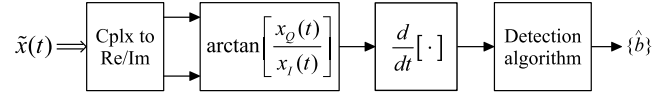


Fig. 15. Complex envelope based binary GFSK demodulator.

### C. $M$ -ary phase-shift keying (MPSK)

An MPSK signal is characterized by  $M$  symbols with equal energies  $E$ , formed by setting  $M$  equally-spaced initial phases of the carrier at the beginning of a symbol [5, pp. 422-434]. The  $i$ -th MPSK symbol, for  $i = 1, \dots, M$ , can be written as

$$s_i(t) = \sqrt{\frac{2E}{T}} \cos\left(2\pi f_c t - \frac{2(i-1)\pi}{M}\right), \quad (35)$$

or using the complex envelope representation obtained through the golden rule, which yields

$$s_i(t) = \text{Re} \left[ \sqrt{\frac{2E}{T}} e^{-j\frac{2(i-1)\pi}{M}} e^{j2\pi f_c t} \right],$$

from where

$$\tilde{s}_i(t) = \sqrt{\frac{2E}{T}} e^{-j\frac{2(i-1)\pi}{M}}. \quad (36)$$

Using (9) with the in-phase and the quadrature components extracted from (36), the MPSK symbols can be rewritten as

$$s_i(t) = \sqrt{\frac{2E}{T}} \cos\left[\frac{2(i-1)\pi}{M}\right] \cos(2\pi f_c t) + \sqrt{\frac{2E}{T}} \sin\left[\frac{2(i-1)\pi}{M}\right] \sin(2\pi f_c t),$$

from where, using (22) with  $N = 2$ , that is,  $s_i(t) = s_{i1}\phi_1(t) + s_{i2}\phi_2(t)$ , it follows that the MPSK base functions are

$$\phi_1(t) = \sqrt{\frac{2}{T}} \cos(2\pi f_c t),$$

$$\phi_2(t) = \sqrt{\frac{2}{T}} \sin(2\pi f_c t).$$

Applying the golden rule, the corresponding complex envelopes can be found to be

$$\tilde{\phi}_1(t) = \sqrt{\frac{2}{T}},$$

$$\tilde{\phi}_2(t) = -j\sqrt{\frac{2}{T}}.$$

Notice, once again, that the energy of the complex envelope of a base function is twice the energy of the corresponding passband function.

The quaternary PSK (QPSK or 4PSK) modulation is considered hereafter as an exemplifying case. The extension to  $M > 4$  is quite straightforward.

The 4PSK modulator can be constructed in light of Fig. 7 and the above results, yielding the diagram shown in Fig. 16.

Substituting  $i = 1, 2, 3, 4$  in (36), the complex envelopes of the 4PSK symbols are obtained as

$$\begin{aligned}\tilde{s}_1(t) &= \sqrt{\frac{2E}{T}}, & \tilde{s}_2(t) &= -j\sqrt{\frac{2E}{T}}, \\ \tilde{s}_3(t) &= -\sqrt{\frac{2E}{T}}, & \tilde{s}_4(t) &= j\sqrt{\frac{2E}{T}},\end{aligned}$$

from where it can be noticed that all symbols have constant amplitudes during a symbol interval  $T$ .

The bit-to-symbol mapping for minimum bit error probability must follow the Gray code, yielding  $00 \Leftrightarrow \tilde{s}_1(t)$ ,  $01 \Leftrightarrow \tilde{s}_2(t)$ ,  $11 \Leftrightarrow \tilde{s}_3(t)$ , and  $10 \Leftrightarrow \tilde{s}_4(t)$ .

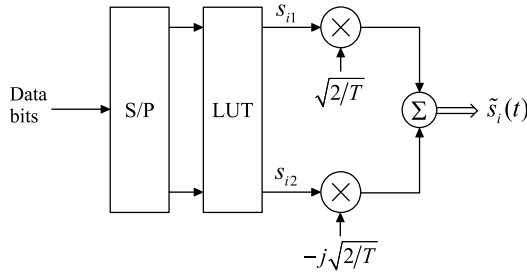


Fig. 16. 4PSK complex envelope based modulator.

Using the complex symbols and base functions, the signal-vector coefficients can be easily determined via (26), yielding

$$\begin{aligned}s_{11} &= \sqrt{E}, & s_{12} &= 0, \\ s_{21} &= 0, & s_{22} &= \sqrt{E}, \\ s_{31} &= -\sqrt{E}, & s_{32} &= 0, \\ s_{41} &= 0, & s_{42} &= -\sqrt{E}.\end{aligned}$$

From these calculations and based on the generalized demodulator given in Fig. 8, the complex envelope based 4PSK demodulator shown in Fig. 17 results. The constants that do not affect performance have been removed. Specifically, the multiplication by  $\hat{\phi}_1^*(t) = \sqrt{2/T}$  in the upper arm of the demodulator is not necessary if the multiplication by  $\hat{\phi}_2^*(t) = j\sqrt{2/T}$  in the lower arm is replaced by the multiplication by  $j$ . Additionally, the signal-vector coefficients can be normalized with respect to  $\sqrt{E}$ . Hence, the inner products of the demodulator become  $z_i = \mathbf{y}^T \mathbf{s}_i / \sqrt{E} = (y_1 s_{i1} + y_2 s_{i2}) / \sqrt{E}$ , for  $i = 1, 2, 3, 4$ , where  $\mathbf{y} = \mathbf{x} / \sqrt{2/T}$ . These relations yield  $z_1 = y_1$ ,  $z_2 = y_2$ ,  $z_3 = -y_1$  and  $z_4 = -y_2$ . Moreover, the subtractions of half of the symbol energies are not necessary, since these energies are all equal to one another. The rest of the demodulator follows Fig. 8 with no further simplification.

#### D. M-ary quadrature amplitude modulation (MQAM)

An MQAM passband signal has phase and amplitude variations that result from the addition of amplitude-modulated quadrature carriers. Hence, the  $i$ -th passband MQAM symbol,  $i = 1, 2, \dots, M$ , can be written as

$$s_i(t) = s_{i1} \sqrt{\frac{2}{T}} \cos(2\pi f_c t) + s_{i2} \sqrt{\frac{2}{T}} \sin(2\pi f_c t), \quad (37)$$

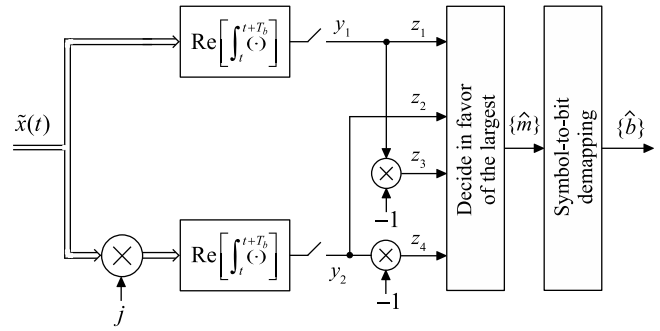


Fig. 17. 4PSK complex envelope based demodulator.

from where it can be noticed that MQAM and MPSK share the same base functions, and that, applying (8) and (9),

$$\tilde{s}_i(t) = s_{i1} \sqrt{\frac{2}{T}} - j s_{i2} \sqrt{\frac{2}{T}}. \quad (38)$$

The coefficients  $s_{i1}$  and  $s_{i2}$  are chosen such that the MQAM signal-vectors are not restricted to lie on a circle, which is the case of MPSK symbols, but instead are placed on a grid in the two-dimensional space, allowing for larger Euclidean distances between symbols when compared to MPSK. These larger distances can be translated into superior performances of the MQAM with respect to MPSK [5, p. 450].

The MQAM family comprises two subcategories usually referred to as square MQAM and non-square MQAM [5, pp. 434-449]. As the names suggest, square MQAM are those with constellations having square shape, whereas non-square MQAM constellations may assume any shape. A typical non-square MQAM constellation has the shape of a cross and, as such, receives the name of cross-constellation. Square MQAM modulations carry an even number of bits per symbol, that is  $M = 2^n$  with  $n \geq 2$  and even. Non-square MQAM modulations carry an odd number of bits per symbol, that is  $M = 2^n$  with  $n \geq 3$  and odd.

In principle, an MQAM complex envelope based modem does not differ too much from its MPSK counterpart: the modulators have two arms and apply the same base functions, differing only in the implementation of the LUT. The demodulators apply the same correlations with the complex conjugated base functions, with the difference that the subsequent subtractions of half the symbol energies must be performed in the case of the MQAM, since this modulation has symbols with different energies. The rest of the demodulator is identical in both modulations.

Nonetheless, the square MQAM can be implemented in an alternative and interesting way, and for this reason it is further explored in the sequel.

The pairs of signal-vector coefficients for the square MQAM can be determined by the Cartesian product<sup>11</sup> between the set  $\psi$  and itself, where  $\psi = \{(2u - \sqrt{M} - 1)(d_{\min}/2)\}$ , for  $u = 1, 2, \dots, \sqrt{M}$ , and where  $d_{\min}$  is the minimum among the distances between all pairs of signal-vectors. In other words, the square MQAM signal-vectors

<sup>11</sup>The Cartesian product between the sets  $X$  and  $Y$  is another set formed by all the pairs  $(x, y)$  such that  $x \in X$  and  $y \in Y$ .

are formed by independent coefficients  $s_{i1}$  and  $s_{i2}$ . As a consequence, the modulator can generate  $s_{i1}$  from one group of  $(\log_2 M)/2 = \log_2 \sqrt{M} = \log_2 L$  input data bits, and  $s_{i2}$  from the other group of  $\log_2 L$  bits, by means of baseband  $L$ -ary pulse amplitude modulation (LPAM). This is illustrated in Fig. 18, where the generalized complex envelope based square MQAM modulator is presented.

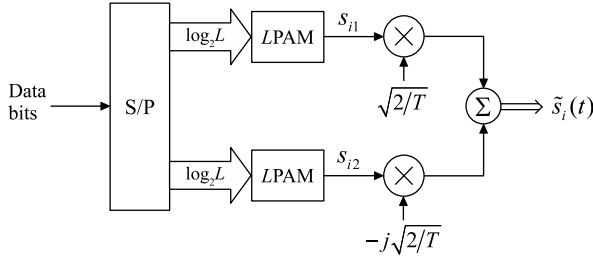


Fig. 18. Square MQAM complex envelope based modulator.

The independence between  $s_{i1}$  and  $s_{i2}$  also allows for estimating each group of  $\log_2 L$  bits independently, by means of two LPAM detectors, as illustrated in Fig. 19. These detectors compare  $y_1$  and  $y_2$ , which are generated in the same way that in the case of the MPSK demodulator, against  $L - 1$  decision thresholds to estimate each group of  $\log_2 L$  bits.

It is worth considering the increased complexity of the MQAM demodulator in comparison with the MPSK, credited to the need for establishing the thresholds shown in Fig. 19 or, equivalently, the received symbol energies in the case of the general MQAM demodulator directly devised from Fig. 8.

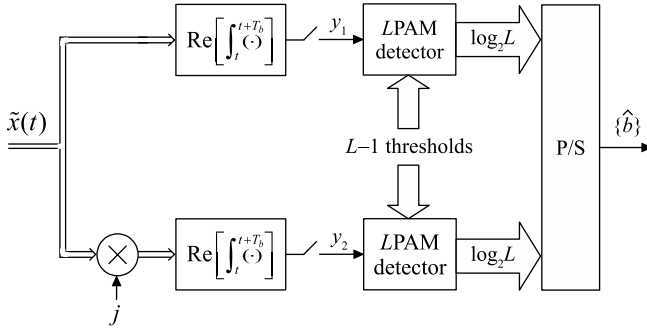


Fig. 19. Square MQAM complex envelope based demodulator.

As an example, consider a 16QAM constellation with  $d_{\min} = 2$ . Then,  $\psi = \{2u - 5\}$ , for  $u = 1, 2, 3, 4$ , yielding  $\psi = \{-3, -1, 1, 3\}$ , which corresponds to the coordinates of the 4PAM signal-vectors in each arm of the modulator. Hence,  $(s_{i1}, s_{i2}) = (-3, -3), (-3, -1), (-3, 1), (-3, 3), (-1, -3), (-1, -1), (-1, 1), (-1, 3), (1, -3), (1, -1), (1, 1), (1, 3), (3, -1), (3, -1), (3, 1), (3, 3)$  are the coordinates of the 16QAM signal-vectors. At the demodulator, assuming for example that the channel attenuation in terms of magnitude is 6 dB, the means of  $y_1$  (which are equal to the means of  $y_2$ ) will be  $-1.5, -0.5, 0.5$  and  $1.5$  volts, meaning that the  $L - 1 = 3$  decision thresholds of the 4PAM detectors will be  $-1, 0$  and  $1$  volt. These thresholds define  $L = 4$  decision regions, each corresponding to 2 bits in the upper arm and other 2 bits in the lower arm, yielding the total of 4 estimated bits for each 16QAM received symbol.

### E. Orthogonal frequency-division multiplexing (OFDM)

In OFDM [33], [34], the input data bit stream is split into  $N_c$  lower rate streams that are mapped onto  $N_c$  modulation symbols<sup>12</sup> and transmitted simultaneously through  $N_c$  orthogonal sub-carriers. An OFDM symbol is the result of multiplexing in frequency the  $N_c$  modulation symbols.

The OFDM symbol has an increased duration with respect to the single-carrier modulation symbol, being less sensitive to the delay spread caused by multipath propagation channels [5, Ch. 3]. As a consequence, ISI is reduced. Furthermore, the bandwidth of each modulated sub-carrier can be made smaller than the coherence bandwidth [5, p. 221] of the channel, resulting in a flat fading per sub-carrier, thus facilitating the equalization process at the receiver. Specifically, when a flat fading per sub-carrier is achieved, the phase compensation and magnitude equalization [35] operates in a sub-carrier basis and is usually referred to as one-tap equalization.

Although the practical implementation of OFDM transceivers makes use of discrete-time inverse and direct fast Fourier transform (IFFT, FFT) operations [36], here it is considered the continuous-time implementation approach to maintain consistence with the complex envelope based modems previously addressed, and to facilitate the understanding of the mathematical modeling [5, pp. 647-656].

A passband OFDM symbol of duration  $T$  can be written as

$$s(t) = \sum_{k=1}^{N_c} \text{Re} \left[ \tilde{s}_k(t) e^{j2\pi f_k^{(c)} t} \right],$$

where  $\tilde{s}_k(t) = s_{Ik}(t) + js_{Qk}(t)$  is the complex envelope of the  $M$ -ary modulation symbol conveyed by the  $k$ -th sub-carrier, and  $f_k^{(c)}$  is the  $k$ -th sub-carrier frequency. The set of all sub-carriers is centered about the frequency  $f_c$ , which is the center of the passband OFDM signal spectrum. The set of the  $k$ -th sub-carrier frequency  $f_k$  such that the whole set of sub-carriers is centered about zero, i.e.,  $f_k = f_k^{(c)} - f_c$ , then

$$s(t) = \text{Re} \left[ \sum_{k=1}^{N_c} \tilde{s}_k(t) e^{j2\pi f_k t} e^{j2\pi f_c t} \right],$$

from where the complex envelope of an OFDM symbol can be identified as

$$\tilde{s}(t) = \sum_{k=1}^{N_c} \tilde{s}_k(t) e^{j2\pi f_k t}. \quad (39)$$

The frequency of the  $k$ -th complex sub-carrier  $e^{j2\pi f_k t}$  in baseband is  $f_k = f_1 + k/T$ , with  $f_1$  being the leftmost (negative) frequency. The separation of  $1/T$  between adjacent sub-carriers guarantees that they are pairwise orthogonal, that is,  $\int_0^T e^{j2\pi f_k t} e^{-j2\pi f_l t} dt = 0$  for all  $i \neq k$ .

Based on (39) and on the concept of frequency multiplexing, which starts with a serial-to-parallel conversion, the complex envelope based OFDM modulator can be constructed according to Fig. 20. The input data bits are converted into  $N_c$  parallel streams, each carrying  $\log_2 M$  bits. Each group of  $\log_2 M$  bits is mapped into the corresponding constellation symbol in terms of complex envelope. Subsequently, the  $N_c$  modulation

<sup>12</sup>Although not rarely considered in the literature, OFDM is not a modulation. Instead, it is a technique that multiplexes symbols generated from a given modulation. Typical modulations used along with OFDM are MPSK and MQAM.

symbols are multiplexed by means of the orthogonal complex exponentials. In this figure, the  $M$ -ary modulators are assumed to be equal to one another, but in general each sub-carrier can convey different numbers of bits per symbol, if needed.

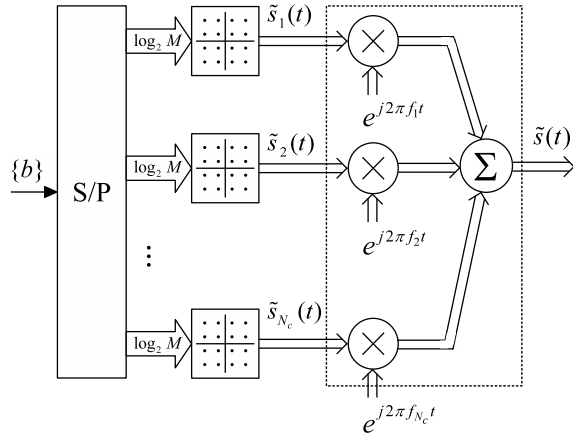


Fig. 20. Complex envelope based OFDM modulator.

To recover the transmitted modulation symbols, the received signal is correlated with  $1/T$  times the complex conjugate of the complex exponentials, as shown in Fig. 21. In the absence of noise or any other impairment, i.e.,  $\tilde{x}(t) = \tilde{s}(t)$ , it can be easily verified that

$$\tilde{s}_k(t) = \frac{1}{T} \int_0^T \tilde{s}(t) e^{-j2\pi f_k t} dt.$$

Subsequently, the  $N_c$  modulation symbols are estimated by means of the appropriate complex envelope demodulator. The estimated symbols are mapped back into the bits that they represent, according to the modulation adopted, and then they are demultiplexed to be delivered to the destination.

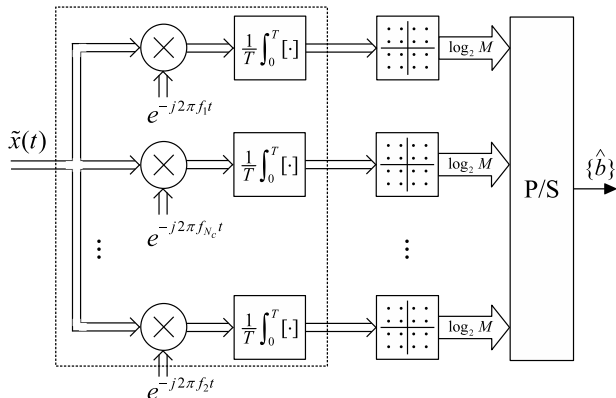


Fig. 21. Complex envelope based OFDM demodulator.

The blocks marked in dashed lines in Figs. 20 and 21 are the ones typically implemented in practice by means of the IFFT and the FFT operations, respectively, along with the necessary A/D, D/A and filtering.

Another typical signal processing operation made to form the final transmitted signal in practice is the addition of a nonzero guard interval to each discrete-time OFDM symbol to protect the signal even more against ISI. The samples corresponding to this guard interval are removed at the receiver.

As a closing-section highlight, it is worth remembering that, for all modems previously considered, the real transmitted signal can be generated in practice from the in-phase and the quadrature components  $s_I(t)$  and  $s_Q(t)$  of the complex envelope based symbols by means of the IQ modulator shown in Fig. 1. This highlight is relevant for the reader to review the connection of the complex envelope modems with the concept of software-defined radios. Analogously, the in-phase and the quadrature components of the received signal can be recovered by means of the IQ demodulator shown in Fig. 2.

## VI. CASE STUDY: SIMULATION OF A 4PSK MODEM OVER A RAYLEIGH FADING CHANNEL

In this Section, the 4PSK complex envelope modem discussed in Subsection V-C has been selected as a representative case for performance analysis via computer simulation.

The simulation has been implemented in the VisSim/Comm software [22], and its diagram is shown in Fig. 22. Random data bits are generated at 1 bit/s, feeding the 4PSK complex envelope modulator, whose internal construction is shown in Fig. 23. This construction follows Fig. 16, for  $T = 2T_b = 2$  seconds. The LUT simply converts each pair of paralleled input bits into the amplitudes of  $s_I(t)$  and  $s_Q(t)$ , which are  $s_{i1}\sqrt{2/T}$  and  $-s_{i2}\sqrt{2/T}$ , respectively, for  $T = 2$  seconds,  $E = 1$  joule, and  $i = 1, 2, 3, 4$ . The resultant LUT mapping is:  $00 \Rightarrow (1, 0)$ ,  $01 \Rightarrow (0, -1)$ ,  $11 \Rightarrow (-1, 0)$ , and  $10 \Rightarrow (0, 1)$ , respectively. Since the simulation sampling frequency is  $f_s = 5$  Hz, each 4PSK symbol is represented by 10 samples, yielding a signal-to-aliasing noise ratio of  $\approx 16.78$  dB [7, p. 88], which is quite high to affect the performance assessment.

The 4PSK complex envelope signal goes through a multiplicative Rayleigh block-fading channel that mimics a slow and flat fading [5, p. 211]. The construction of this channel follows Fig. 24, where a case block selects between the pure AWGN channel and the AWGN plus Rayleigh fading channel. The Rayleigh random variable is sampled and held at the symbol rate, guaranteeing a constant fading magnitude during a whole symbol; this condition is necessary to verify the simulation according to the theoretical symbol or bit error probability, which subsumes such condition. The samples of the Rayleigh random variable feed a magnitude-phase to complex conversion block, with zero phase in order to simulate the total phase rotation compensation made in coherent detection.

Subsequently to the multiplicative fading channel, the AWGN block adds the thermal noise whose  $E/N_0$  is automatically set according to the average complex signal power  $P = 2E/T = 1$  watt, and the symbol rate  $R = 0.5$  symbol per second. Five values of  $E/N_0$  are simulated, namely 3, 5, 7, 9, 11 dB, yielding  $E_b/N_0 = 0, 2, 4, 6, 8$  dB.

The bottom part of Fig. 22 is the complex envelope demodulator whose construction follows Fig. 17. It is worth highlighting the exchange in position of the inputs 3 and 4 of the scalar-to-vector (S->V) block, which is a consequence of the Gray symbol-to-bit mapping [5, p. 380]. The blocks S->V, maximum vector element identification (maxElement) and the subtraction by 1 (\$1-1) compose the block that decides in favor of the largest input in Fig. 17. The parallel-to-serial

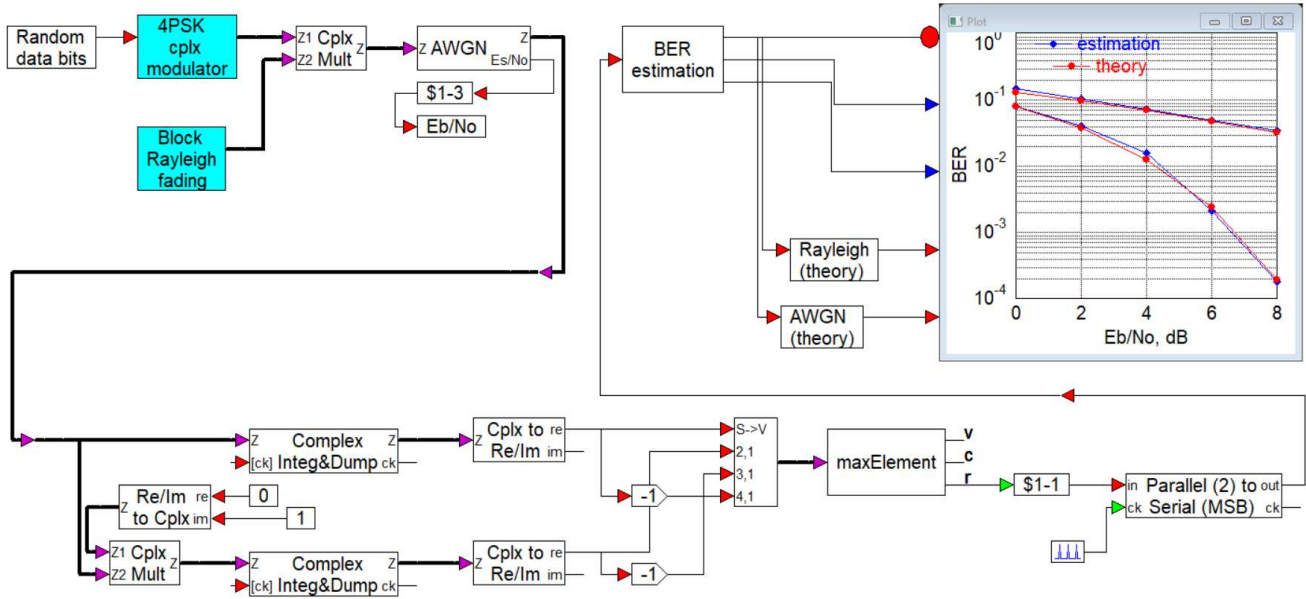


Fig. 22. VisSim/Comm diagram for simulating the 4PSK complex envelope modem over the pure AWGN and the AWGN plus Rayleigh fading channels. The BER versus  $E_b/N_0$  graph is better viewed in color.

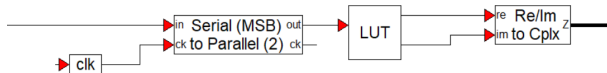


Fig. 23. VisSim/Comm diagram for the 4PSK complex envelope modulator.

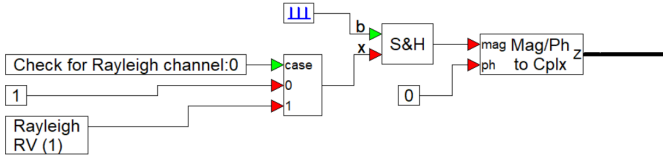


Fig. 24. VisSim/Comm diagram for the Rayleigh block-fading channel.

block maps the estimated symbol index into the estimated data bits, which are serially delivered to the bit error rate (BER) estimation block, from which the BER versus  $E_b/N_0$  graph is plotted. Each BER estimate is computed from a fixed preselected number of bit errors. The numbers of errors set in the present simulation are 300, 200, 150, 100, 80, respectively for  $E_b/N_0 = 0, 2, 4, 6, 8$  dB.

The estimated BERs over the AWGN and the Rayleigh fading channels are plotted along with the corresponding theoretical bit error probabilities. In the case of the AWGN channel, the exact theoretical symbol error probability for the  $M$ PSK modulation with coherent detection is given in [20, Eqn. (8.23)], which for  $M = 4$  specializes to

$$P_s = \frac{1}{\pi} \int_0^{3\pi/4} \exp\left(-\frac{E_b}{N_0 \sin^2 \theta}\right) d\theta. \quad (40)$$

The exact symbol error probability of coherent  $M$ PSK over a slow and flat Rayleigh fading channel is given in [20, Eqn. (8.113)], which for the 4PSK modulation yields

$$P_s = \frac{3}{4} \left\{ 1 - \frac{4}{3\pi} \sqrt{\frac{\gamma_b}{1 + \gamma_b}} \left[ \frac{\pi}{2} + \tan^{-1} \left( \sqrt{\frac{\gamma_b}{1 + \gamma_b}} \right) \right] \right\}, \quad (41)$$

where  $\gamma_b = \mathbb{E}\{\alpha^2\}E_b/N_0$  is the average signal-to-noise ratio per bit, with  $\mathbb{E}\{\alpha^2\}$  being the second moment of the fading envelope, which is unitary in the simulation at hand.

Since the Gray mapping is adopted, the approximate theoretical bit error probabilities that are plotted in Fig. 22 are given by  $P_b = P_s / \log_2 M = P_s / 2$ , with  $P_s$  coming from (40) and (41) for the AWGN and the Rayleigh channel, respectively. The graph shows close agreement between the estimated BERs and the associated theoretical curves, which validates the simulation. A procedure similar to the one described in this section can be used in the case of the remaining modems considered in the previous section.

As a complimentary simulation result, Fig. 25 shows the estimated PSD of the simulated complex envelope 4PSK signal at the output of the modulator in Fig. 22. This PSD is practically equal to the theoretical one [5, p. 431]. Notice that the spectrum span goes from 0 to 2.5 Hz, a consequence of the simulation sampling frequency  $f_s = 5$  Hz. Moreover, the spectral nulls are located at integer multiples of  $1/T$ , which is consistent with the symbol rate  $R = 1/T = 0.5$  symbol per second. Additionally, observe that the spectrum is not confined (unless by the natural simulation limit of  $f_s/2$ ), which is, according to the uncertainty principle of the Fourier transform, a consequence of the confined rectangular symbol waveform.

## VII. FILTERING

There is not a single approach for filtering modulated signals at the transmitter and at the receiver of a digital communication system. At the transmitter, it can be made in baseband, acting independently on  $s_I(t)$  and  $s_Q(t)$ , or in passband, acting on  $s(t)$ , or both. In the former case, two LPFs are needed, whereas in the latter case one band-pass filter (BPF) must be applied. Since a LPF is often easier to design than its band-pass counterpart, the adoption of baseband filtering is

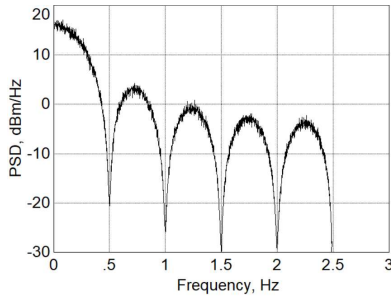


Fig. 25. Estimated power spectral density of the baseband 4PSK signal.

prevalent in practice. However, there are cases in which a BPF is needed in addition to LPFs, for example when the modulated signal goes through nonlinear amplification. The nonlinearity produces spectral regrowth [5, p. 511], demanding additional filtering to keep the power spectrum density compliant with the specified radiated spectral mask. Filtering is also necessary for pulse shaping in order to avoid ISI. A band-pass receive filter is normally applied to limit the signal spectrum entering the receiver. Low-pass receive filters, on the other hand, typically are the twins of the transmit filters acting to control ISI. This section explores these facets.

#### A. Mapping a passband filter response into baseband

From the complex envelope representation theory applied to linear systems, it is known that if a passband filter impulse response  $h(t)$  is written in the complex envelope form as  $\tilde{h}(t)$ , the complex envelope of the output signal,  $\tilde{b}(t)$ , is determined by a scaled convolution between the complex envelope of the input signal,  $\tilde{a}(t)$ , and  $\tilde{h}(t)$  [10], [21]. Specifically,  $\tilde{b}(t) = \frac{1}{2}[\tilde{a}(t) * \tilde{h}(t)]$ . Since  $\tilde{a}(t) = a_I(t) + ja_Q(t)$ ,  $\tilde{h}(t) = h_I(t) + jh_Q(t)$ , and  $\tilde{b}(t) = b_I(t) + jb_Q(t)$ , then

$$\begin{aligned} 2b_I(t) &= a_I(t) * h_I(t) - a_Q(t) * h_Q(t), \\ 2b_Q(t) &= a_I(t) * h_Q(t) + a_Q(t) * h_I(t), \end{aligned}$$

meaning that four real convolutions are needed to compute the real and the imaginary parts of a complex convolution.

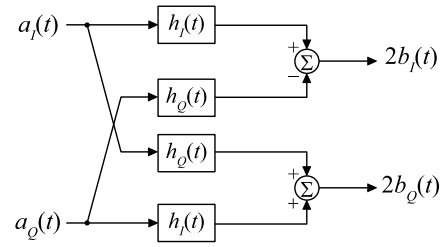
Additionally, if  $H(f) = \int_{-\infty}^{\infty} h(t)e^{-j2\pi ft} dt$  is the frequency response of a filter in passband form, the frequency-domain complex envelope  $\tilde{H}(f) = H_I(f) + jH_Q(f)$  can be determined as follows: Since  $h_I(t) = \text{Re}[\tilde{h}(t)]$  and  $h_Q(t) = \text{Im}[\tilde{h}(t)]$ , then  $h_I(t) = [\tilde{h}(t) + \tilde{h}^*(t)]/2$  and  $h_Q(t) = [\tilde{h}(t) - \tilde{h}^*(t)]/(2j)$ . The Fourier transform of  $\tilde{h}^*(t)$  is  $\int_{-\infty}^{\infty} \tilde{h}^*(t)e^{-j2\pi ft} dt = [\int_{-\infty}^{\infty} \tilde{h}(t)e^{j2\pi ft} dt]^* = \tilde{H}^*(-f)$ . Then,

$$\begin{aligned} H_I(f) &= \frac{1}{2}[\tilde{H}(f) + \tilde{H}^*(-f)], \\ H_Q(f) &= \frac{1}{2j}[\tilde{H}(f) - \tilde{H}^*(-f)], \end{aligned}$$

finally yielding

$$\tilde{H}(f) = \frac{1}{2}[\tilde{H}(f) + \tilde{H}^*(-f)] + \frac{1}{2j}[\tilde{H}(f) - \tilde{H}^*(-f)]. \quad (42)$$

Hence, if a BPF with frequency response  $H(f)$  is desired,  $\tilde{H}(f)$  is determined from (42), and  $\tilde{h}(t) = h_I(t) + jh_Q(t)$  is computed from the inverse Fourier transform of  $\tilde{H}(f)$ . The filtering of the complex envelope  $\tilde{a}(t) = a_I(t) + ja_Q(t)$  is then performed as illustrated in Fig. 26.


 Fig. 26. Filtering the complex envelope  $\tilde{a}(t) = a_I(t) + ja_Q(t)$  of the real passband signal  $a(t)$ .

#### B. Pulse shaping for zero ISI

The Nyquist criterion for baseband ISI-free transmission [5, p. 312] states that if the impulse response of the system that comprises the transmit filter, the channel, and the receive filter has nulls at integer multiples of the symbol duration  $T$ , the samples collected at the output of the receive filter are free from ISI. This is guaranteed if the channel is almost distortionless in the transmitted signal bandwidth, and if the overall frequency responses of the filters exhibit vestigial symmetry around  $1/(2T)$  hertz [5, p. 313]. Among the infinitely many possibilities of satisfying this condition, the raised cosine spectrum is the most used in practice. This means that the transmit and receive filters must be of the type root raised cosine (RRC), which is nothing more than the square-root of the raised cosine spectrum. By doing so, not only the ISI is handled, but also the white noise. This is owed to the fact that the transmit filter acts as a pulse-shaping filter (PSF), and the receive filter acts as a matched filter (MF) [5, p. 284].

Assuming that it is intended to apply low-pass PSFs at the transmitter, there is no need for doing filtering like in the case of Fig. 26. The in-phase and the quadrature signals can be filtered independently, as illustrated by Fig. 27 in the context of SDRs. This illustration is for didactic purposes only, since in practice it is more convenient to implement the filters also in the digital domain. Recall that it is also common to implement the up-conversion, at least from baseband to IF, digitally.

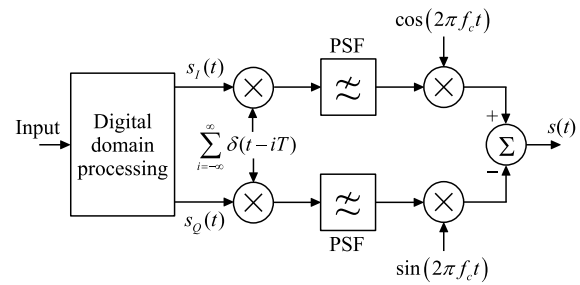


Fig. 27. Simplified block diagram of an SDR modulator with baseband pulse shaping. In practice, the PSFs are also implemented in the digital domain.

In Fig. 27 it is subsumed that  $s_I(t)$  and  $s_Q(t)$  are constant during the symbol interval, since the role of the multiplications by the impulse train is to generate impulse-like short duration pulses at the input of the filters so that the output signal closely approximates the impulse responses scaled by the amplitudes of  $s_I(t)$  and  $s_Q(t)$ . Nonetheless, if  $s_I(t)$  and  $s_Q(t)$  are not constant during the symbol interval, as in the case of MFSK signals for example, baseband filtering can still be performed,

but this is usually the case for spectrum control only, not to combat ISI.

It is interesting to realize that the receiving-end counterpart of the modulator shown in Fig. 27 can benefit from the need for matched filtering, which can be accomplished by replacing the LPFs shown in Fig. 2 by filters identical to the PSFs used in the modulator. However, in this case it shall not be intended to recover  $s_I(t)$  and  $s_Q(t)$ , but instead to have the samples of the filters' output signals free from ISI. Indeed, the outputs of the MFs will not be equal to  $s_I(t)$  and  $s_Q(t)$  generated in the modulator of Fig. 27, since these filters will unavoidably produce considerable time spreading.

### C. Pulse shaping in the generalized complex envelope modulator and demodulator

Assume that the PSFs designed to combat ISI have identical real impulse responses denoted by  $p(t)$ . Following a reasoning analogous to the one adopted in the case of Fig. 27, the generalized complex envelope based modulator given in Fig. 7 is converted into the one shown in Fig. 28.

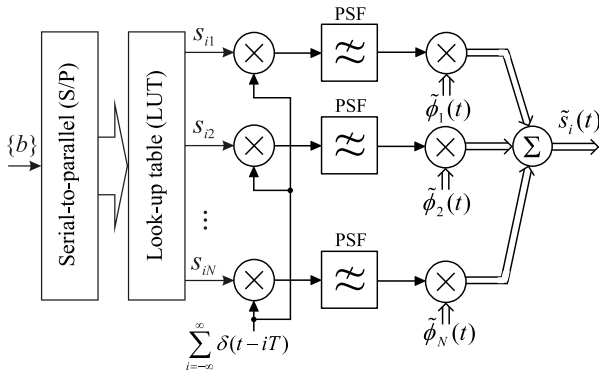


Fig. 28. Generalized complex envelope based modulator with pulse shaping.

If  $s_I(t)$  and  $s_Q(t)$  are constant within the symbol interval, the PSFs acting on the signal-vector coefficients as shown in Fig. 28 are not needed, and the process adopted in Fig. 7 can be used instead, that is,  $s_I(t)$  and  $s_Q(t)$  are multiplied by an impulse train and the results go through a pair of PSFs.

It must be emphasized that, even though the signal-vector coefficients  $s_{ik}$ ,  $i = 1, 2, \dots, M$ ,  $k = 1, 2, \dots, N$  are determined using energy signals, the linear combination (25) also applies when the base functions are shaped by pulses lasting more than the symbol interval, which is the case of RRC pulses and other ones designed to prevent ISI. An immediate consequence of such pulse shaping is that the demodulator must adopt an MF replacing each correlator in order to capture the entire received symbol energy.

From the digital communication theory, and according to the modulator in Fig. 28, the MFs must have impulse responses  $\kappa p(\tau - t)\tilde{\phi}_k^*(\tau - t)$ , where  $\tau$  is a suitable delay enough for producing causal filters, and  $\kappa$  is any nonzero scale factor. Since the delay and the scaling do not affect performance, from the mathematical viewpoint the impulse response of the  $k$ -th MF can be written in the compact form  $p(-t)\tilde{\phi}_k^*(-t)$ .

Taking into account that the MF and the correlator share the same signal-to-noise ratio at the sampling instant, (27) can be

invoked again to conclude that the MF output samples are the real part of the convolution between the complex envelope of the input and the complex envelope of the system impulse response. Hence, it follows that the observed vector elements  $y_1, y_2, \dots, y_N$ , which are scaled versions of  $x_1, x_2, \dots, x_N$  in the demodulator of Fig. 8, can be obtained by replacing the correlators by MFs with impulse responses  $p(-t)\tilde{\phi}_k^*(-t)$ , yielding the generalized demodulator shown in Fig. 29. The outputs of the MFs are sampled every  $T$  seconds, and the results are processed in the same way that in the case of the demodulator given in Fig. 8.

### D. Filter design in the context of multirate systems

The implementation of SDRs often involves different sample rates in order to adequate the signal processing tasks to the signal bandwidth in each part of the system, as well as to improve performance, reduce the costs or facilitate the design of some device or subsystem. Systems or devices that operate with multiple sample rates are usually referred to as multirate systems or multirate devices [9, Ch. 10]. Examples are the DUC and DDC mentioned in Section II, and the important class of multirate digital filters [13].

Although the design and implementation of digital filters in the context of SDRs is beyond the scope of this tutorial, it might be useful to the reader to know at least which are, and where to find the fundamentals behind such topic.

The theory about designing digital filters is commonly addressed in specific tutorial articles or books [37], [38], and in books on digital (or discrete-time) signal processing [39]. On the other hand, one of the most important concepts associated to the implementation of multirate systems or devices, especially digital filters, is the sample rate conversion by means of down-sampling and up-sampling [13]. In simple terms, the former removes samples of the signal, as if it were sampled in a lower rate, and the latter inserts interpolated samples in-between the original ones, as if the signal were sampled in a higher rate. Down-sampling and up-sampling often make it simpler the implementation of digital filters, reducing costs, energy consumption and circuit or chip area.

## VIII. CONCLUSIONS

This tutorial addressed the basic theory of complex envelope based modems. It has been shown that this theory is fundamental for understanding and developing simulations of communication systems and software-defined radios. In simulations, it helps reducing the sampling rates, consequently reducing the computation burden and simulation time. In software-defined radios, it launches the basis for creating the main building blocks of radios in which most of the tasks are performed in the digital domain, in a re-configurable fashion.

The author hopes that this work can be of help for the readers to pave the way for more advanced studies in this beautiful area, which is at the same time vast and challenging.

## REFERENCES

- [1] M. C. Jeruchim, P. Balaban, and K. S. Shanmugan, Eds., *Simulation of Communication Systems: Modeling, Methodology and Techniques*, 2nd ed. Kluwer Academic Publishers, 2000.

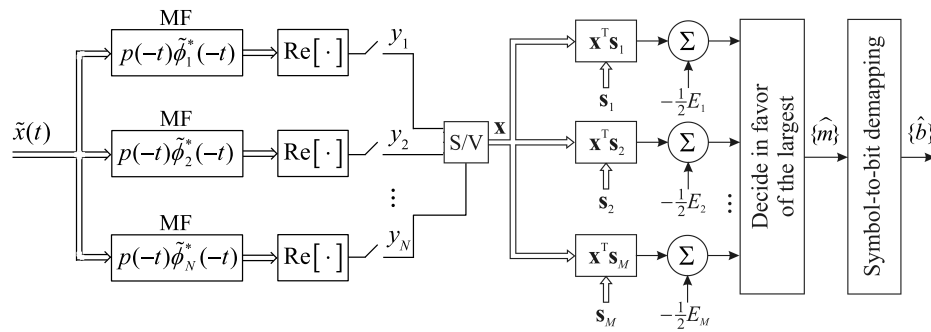


Fig. 29. Generalized complex envelope based maximum-likelihood demodulator with matched filters.

[2] H. Van Trees, *Detection, Estimation, and Modulation Theory, Part III: Radar-Sonar Signal Processing and Gaussian Signals in Noise*. John Wiley & Sons, 2004.

[3] J. G. Proakis, *Digital Communications*. McGraw-Hill, 2001.

[4] S. Haykin, *Communication Systems*, 5th ed. Wiley Publishing, 2009.

[5] D. A. Guimarães, *Digital Transmission: A Simulation-Aided Introduction with VisSim/Comm*. Springer-Verlag, 2009, doi: 10.1007/978-3-642-01359-1.

[6] R. G. Vaughan, N. L. Scott, and D. R. White, "The theory of bandpass sampling," *IEEE Trans. Signal Process.*, vol. 39, no. 9, pp. 1973–1984, Sep. 1991, doi: 10.1109/78.134430.

[7] W. Tranter, K. Shanmugan, T. Rappaport, and K. Kosbar, *Principles of Communication Systems Simulation with Wireless Applications*, 1st ed. Prentice Hall, 2003.

[8] H. Harada and R. Prasad, *Simulation and Software Radio for Mobile Communications*. Artech House, Inc., 2002.

[9] T. J. Roupahel, *RF and Digital Signal Processing for Software-Defined Radio: A Multi-Standard Multi-Mode Approach*. Newnes, 2008.

[10] G. Kolumban, T. I. Krebesz, and F. C. M. Lau, "Theory and application of software defined electronics: Design concepts for the next generation of telecommunications and measurement systems," *IEEE Circuits Syst. Mag.*, vol. 12, no. 2, pp. 8–34, 2012, doi: 10.1109/MCAS.2012.2193435.

[11] A. Wyglinski and D. Pu, *Digital Communication Systems Engineering with Software-Defined Radio*. Artech House, 2013.

[12] A. Wyglinski, R. Getz, T. Collins, and D. Pu, *Software-Defined Radio for Engineers*. Artech House, 2018.

[13] F. J. Harris, *Multirate Signal Processing for Communication Systems*. Prentice Hall PTR, 2004.

[14] F.-L. Luo (Ed.), *Digital Front-End in Wireless Communications and Broadcasting: Circuits and Signal Processing*. Cambridge University Press, 2011, doi: 10.1017/CBO9780511744839.

[15] T. Schenk, *RF imperfections in high-rate wireless systems: impact and digital compensation*. Springer Science and Business Media, 2008, doi: 10.1007/978-1-4020-6903-1.

[16] B. Razavi, "Design considerations for direct-conversion receivers," *IEEE Trans. Circuits Syst.*, vol. 44, no. 6, pp. 428–435, Jun. 1997, doi: 10.1109/82.592569.

[17] S. Arar, "Basics of digital down-conversion in DSP," jun 2018. [Online]. Available: {https://www.allaboutcircuits.com/technical-articles/dsp-basics-of-digital-down-conversion-digital-signal-processing/}

[18] —, "Articles by Steve Arar," oct 2019. [Online]. Available: {https://forum.allaboutcircuits.com/ubs/the-list-of-my-articles-on-aac.1135/}

[19] D. Gabor, "Theory of communication," *Journal of the Institution of Electrical Engineers*, vol. 93, no. 26, pp. 429–457, November 1946.

[20] M. Simon and M. Alouini, *Digital Communication over Fading Channels*. Wiley, 2005, doi: 10.1002/0471715220.

[21] M. E. Halabi, "CCE401: communication systems (course notes)," nov 2019. [Online]. Available: {https://mustafa-halabi.appspot.com/CCE401.html}

[22] Altair Engineering, Inc. (former Visual Solutions, Inc.), "VisSim: A graphical language for simulation and model-based embedded development," nov 2015. [Online]. Available: http://www.vissim.com/products/vissim/comm.html.

[23] Mathworks, Inc., "Simulink: Simulation and model-based design platform," nov 2019. [Online]. Available: https://www.mathworks.com/products/simulink.html

[24] A. Giordano and A. Levesque, *Modeling of Digital Communication Systems Using Simulink*. John Wiley & Sons, 2015.

[25] GNU Radio Foundation, Inc., "GNU Radio: The Free & Open Software Radio Ecosystem," Dec 2019. [Online]. Available: https://www.gnuradio.org/

[26] D. Valerio, "Open source software-defined radio: A survey on GNU Radio and its applications," *Forschungszentrum Telekommunikation Wien, Vienna, Technical Report FTW-TR-2008-002*, Aug. 2008.

[27] National Instruments Corporation, "Introduction to Bluetooth Device Testing: From Theory To Transmitter and Receiver Measurements," sep 2016. [Online]. Available: {http://download.ni.com/evaluation/rf/intro\_to\_bluetooth\_test.pdf}

[28] Bluetooth Special Interest Group (SIG), "Bluetooth Core Specification Version 5.1," nov 2019. [Online]. Available: {https://www.bluetooth.com/specifications/bluetooth-core-specification/}

[29] T. Švedek, M. Herceg, and T. Matic, "A simple signal shaper for GMSK/GFSK and MSK modulator based on sigma-delta look-up table," *Radioengineering*, 06 2009.

[30] F. Li, "Simulation multi-moteurs multi-niveaux pour la validation des spécifications système et optimisation de la consommation," Mars 2016, D.Sc. Thesis, Nice Sophia Antipolis University. [Online]. Available: http://www.theses.fr/2016NICE4008

[31] A. Abdallah, A. Nsour, M. Zohdy, and J. Li, "GFSK demodulation using sequential Monte Carlo technique," *IEEE Wireless Commun. Lett.*, vol. 4, no. 6, pp. 621–624, Dec 2015, doi: 10.1109/LWC.2015.2476460.

[32] M. Messai, G. Colavolpe, K. Amis, and F. Guilloud, "Robust detection of binary CPMs with unknown modulation index," *IEEE Commun. Lett.*, vol. 19, no. 3, pp. 339–342, March 2015, doi: 10.1109/LCOMM.2015.2390230.

[33] S. B. Weinstein, "The history of orthogonal frequency-division multiplexing [history of communications]," *IEEE Commun. Mag.*, vol. 47, no. 11, pp. 26–35, November 2009, doi: 10.1109/MCOM.2009.5307460.

[34] T. Hwang, C. Yang, G. Wu, S. Li, and G. Li, "OFDM and its applications: A survey," *IEEE Trans. Veh. Technol.*, vol. 58, pp. 1673–1694, 06 2009, doi: 10.1109/TVT.2008.2004555.

[35] W. G. Jeon, K. H. Chang, and Y. S. Cho, "An equalization technique for orthogonal frequency-division multiplexing systems in time-variant multipath channels," *IEEE Trans. Commun.*, vol. 47, no. 1, pp. 27–32, Jan 1999, doi: 10.1109/26.747810.

[36] S. Weinstein and P. Ebert, "Data transmission by frequency-division multiplexing using the discrete Fourier transform," *IEEE Trans. Commun. Technol.*, vol. 19, no. 5, pp. 628–634, Oct 1971, doi: 10.1109/TCOM.1971.1090705.

[37] L. Milic, *Multirate Filtering for Digital Signal Processing: MATLAB Applications*. IGI Publishing, 2008, doi: 10.4018/978-1-60566-178-0.

[38] A. Antoniou, *Digital Filters: Analysis, Design, and Signal Processing Applications*. McGraw-Hill Education, 2018.

[39] A. V. Oppenheim and R. W. Schaffer, *Discrete-Time Signal Processing*, 3rd ed. Prentice Hall, 2009.



**Dayan Adionel Guimarães** received the Ph.D. degree in Electrical Engineering from the State University of Campinas, Unicamp, Brazil, in 2003. He is currently a Senior Lecturer and Researcher with the National Institute of Telecommunications, Inatel, Brazil. His research interests are fixed and mobile wireless communications, radio propagation, simulation of digital communication systems, spectrum sensing for cognitive radio, and convex optimization and signal processing applied to communications.